In presenting this thesis in partial fulfillment of the requirements for an advanced degree at Idaho State University, I agree that the Library shall make it freely available for inspection. I further state that permission to download and/or print my thesis for scholarly purposes may be granted by the Dean of the Graduate School, Dean of my academic division, or by the University Librarian. It is understood that any copying or publication of this thesis for financial gain shall not be allowed without my written permission.

Signature _____

Date _____

A Study of Electron Accelerator Based Photon&Neutron Production and Applications to Nuclear Transmutation Technologies

by

Mayir Mamtimin

A dissertation

submitted in partial fulfillment

of the requirements for the degree of

Doctor of Philosophy in the Department of Physics

Idaho State University

July 2014

To the Graduate Faculty:

The members of the committee appointed to examine the dissertation of Mayir Mamtimin (Mayierjiang Maimaitimin) find it satisfactory and recommend that it be accepted.

_____
Frank Harmon, Ph.D.
Major Advisor

_____
George Imel, Ph.D.
Committee Member

_____
Khalid Chouffani, Ph.D.
Committee Member

_____
Eddie Tatar, Ph.D.
Committee Member

_____
Daniel Hummel, Ph.D.
Graduate Faculty Representative

Soyumluk ayalim Kadirya we omak oghlum Arslan'gha beghishlaymen!

Acknowledgments

I would like to express my gratitude to my adviser, Dr. Harmon at the Idaho Accelerator Center, Idaho State University, for his guidance, encouragement and inspiration during my study. Thanks for providing such a caring, supportive yet professional working environment. It was my honor to work with you. In my culture, it is suitable to describe you as a caring father.

I want to thank Dr. Starovoitova for her help, instruction and friendly support from the beginning of my journey here in Pocatello. It was my privilege to have you as my adviser and my friend. In my culture, it is suitable to describe you as a caring sister.

Special thanks to Dr. Imel for his support, guidance and constant help during this project. I would like to express my gratitude towards Dr. Chouffani for his kind help and support. Thank for Dr. Tatar for his time and support during my dissertation.

I would like to thank all the faculty and staff at the Physics department for offering such a warm environment to study and work.

I would like to thank all the friends for the help and support.

Contents

List of Figures

List of Tables

Abstract

This work is a continuation of research and development conducted at the Idaho Accelerator Center on intense photon/neutron sources driven by electron accelerators. Applications of such sources include nuclear activation analysis, isotope production, non-destructive testing, and nuclear fuel cycle investigations.

A new concept of a mixed photon/neutron irradiation field is introduced and explored in this work. Using both photons and neutrons to create a mixed radiation field can potentially improve the transmutation efficiency of selective long-lived fission products (LLFP), particularly ^{129}I. Mixed field transmutation technologies can also be applied to the production of certain high value medical and industrial radioisotopes such as ^{47}Sc and ^{64}Cu.

Electron induced photon/neutron radiation field strength depends on electron beam parameters, as well as the converter material and geometry. In this study, optimization conditions for a 40 MeV electron beam induced single (photon) or mixed (photon and neutron) radiation fields are addressed. Computer simulations and experiments were conducted to develop an efficient transmutation technique using high power electron accelerators. We have demonstrated that, under optimum single or mixed field production conditions, accelerator-driven photonuclear reactions can be practical for many applications, including radioisotope production and nuclear waste transmutation.

Chapter 1

Introduction

1.1 Background

Bremsstrahlung photons, produced by the interaction of electrons with a high Z material, have a unique continuous energy spectrum which can be "tuned" to some extent by electron beam energy and converter geometry. These photons can be copiously produced by electron accelerators. At relativistic electron energies, above an MeV or so, highly forward directed photon beams are produced [1]. Bremsstrahlung photons generated by electron accelerators have enabled many radiographic, medical, material, and industrial applications, including non-destructive testing and imaging techniques [2–4].

Accelerator based intense radiation fields of photons and neutrons made nuclear activation analysis methods feasible at small facilities around the world. In nuclear activation analysis techniques, neutral or charged particles induce radioactivity in interrogated material. By analyzing the radiation spectrum, types of nuclear interactions can be determined and the elemental content of the material can be quantified. An emergent technology is the use of photons for transmutation. The secondary nuclei produced often have useful properties and can be used as medical or industrial isotopes and perhaps in managing other fission products.

Numerous studies have been carried out on the use of nuclear reactor based neutron sources and Spallation Neutron Sources (SNS) for transmutation technologies [5, 6]. There is also an increasing number of studies regarding transmuting long lived fission products (LLFP) to short-lived isotopes by accelerator-driven intense photon or neutron radiation fields [7–11]. These latter studies have shown the feasibility of linac based transmutation

technologies and their potential for cost effective solutions to long term waste management issues [12].

Multi-kilowatt electron accelerator driven sources with beam energies ∼40 MeV can produce energetic photons (10 to 40 MeV) which couple strongly with the giant dipole resonance (GDR) region in nuclei to produce particle emission and hence transmutation reactions (the term "GDR-photons" is used in the rest of the dissertation to refer to the photons with energies between 10 to 40 MeV). The total photo-absorption cross-section in the GDR region is typically dominated by neutron emission reactions. A proper converter/target design can provide more than 10^{13} GDR-photons and 10^{12} fast fission spectrum neutrons/cm^2/s per kW of electron beam power [13]. As a result, radiation fields of photons, neutrons, or both can be produced in which ratios and energy distributions of particles may be varied by electron beam energy and converter design. Based on the optimum production of radiation fields and the nuclear properties of nuclides, nuclear waste transmutation and radioisotope production techniques can be developed .

Used nuclear fuels and related recycling products contain uranium, transuranics (TRU), and fission products (FP) [14]. Unlike the first two, the FP do not hold any recycling value and are the major contributors to radiotoxicity levels in used fuel handling scenarios as they represent true nuclear waste in used fuel compositions (Appendix B). For efficient nuclear waste storage strategies targeting transitions from geological time scales to engineering time scales, it is desirable to explore feasible ways through which the radiotoxicity of the FP stream can be minimized to reduce the environmental burden. This can be accomplished if a significant amount of the most radiotoxic FP nuclides can be transmuted into stable species or species with shorter half-lives. It is also clear that transmutation carried out with irradiations involving fission produced neutrons will only add to the FP burden, which suggests accelerators with photonuclear methods as a possible transmutation driver. Photonuclear reactions, integrated over a broad bremsstrahlung spectrum, can yield significant transmutation, as demonstrated by isotope production reported by a number of researchers [15], including ongoing work at the Idaho Accelerator Center.

Transmutation includes many nuclear processes, but it basically involves converting one isotope to another by removing a single (or multiple) nucleon(s) from a nucleus or by adding a single (or multiple) nucleon(s) to a nucleus. Of particular interest in this work is applying transmutation phenomena to problems in nuclear waste management and production of useful radioisotopes. In the former case the interest is in using transmutation to reduce the environmental burden of the LLFP ^{129}I (10^7 year half-life) and ^{99}Tc (10^5 year half-life). These nuclei are the major risk/dose components of the LLFP, and are the dominant considerations for sustainable long-term nuclear waste management schemes [16–18]. These nuclides can be transmuted to shorter half-life species by (n,γ) and (γ,n) reactions. For example, the ^{99}Tc(n,γ)^{100}Tc reaction results in ^{100}Tc which has a 15.8 second half-life, the ^{129}I(n,γ)^{130}I reaction results in ^{130}I which has a 12.36 hour half-life, and the ^{129}I(γ,n)^{128}I reaction results in ^{128}I which has a 25 minute half-life.

Widely used medical and industrial radioisotopes are mainly produced by nuclear reactors. However, continuous shutdowns, both scheduled and accidental, demonstrate that the supply of cheap, subsidized reactor-produced isotopes is no longer reliable and new accelerator-based production methods need to be developed. Argonne National Laboratory (ANL), the IAC, and other research facilities have been developing linear accelerator driven medical isotope production systems (MIPS) [19], which demonstrate the feasibility of photoproduction of radioisotopes.

Radioisotopes like ^{47}Sc, ^{64}Cu, ^{99}Mo, ^{192}Ir and many others can be produced by mixed field transmutation, where both photon and neutron radiation fields can effectively create the above nuclides from their stable parents [21]. In this work, as a proof of principle, we performed the feasibility study of electron accelerator based production of ^{47}Sc and ^{64}Cu. These radioisotopes were chosen because of their suitable nuclear properties and an increasing demand for their use in radioimmunotherapy.

^{47}Sc, being a β^- emitter, can be used for labeling hormones and other biological substances for radioimmunotherapy and other related assay procedures. Natural scandium contains only one isotope, ^{45}Sc. Although current supply is mainly produced by

neutron capture of ^{47}Ti, it is difficult to produce in the carrier-free state by means of either a cyclotron or a reactor. However, it can be produced easily with the use of an electron accelerator. For the ^{47}Sc production, the available photon and photoneutron induced reactions are ^{48}Ti(γ,p)^{47}Sc, ^{49}Ti(γ,pn)^{47}Sc, ^{50}Ti(γ,p2n)^{47}Sc, ^{51}Ti(γ,α)^{47}Sc, and ^{47}Ti(n,p)^{47}Sc. Among them, the most useful photonuclear reaction are the ^{48}Ti(γ,p)^{47}Sc and ^{47}Ti(n,p)^{47}Sc due to relatively high parent isotope abundances (74% and 7%) and the reaction cross sections.

^{64}Cu is another popular medical isotope. Due to its unique decay properties (it is both β^+ and β^- emitter), ^{64}Cu can simultaneously be used for PET imaging and therapy. Currently, ^{64}Cu is mainly produced by reactors and cyclotrons via the ^{64}Zn(n,p)^{64}Cu and ^{64}Ni(p,n)^{64}Cu. In this work, electron accelerator based production of ^{64}Cu is investigated via ^{65}Cu(γ,n)^{64}Cu and ^{63}Cu(n,γ)^{64}Cu reactions, using the mixed-field irradiation scheme.

1.2 Objectives

The objective of this work is to verify whether or not photonuclear processes based on the excitation of the GDR such as (γ,xn) ,(γ,p) and other gamma-induced reactions, can be used for transmutation purposes. Two potential practical applications of interest are:

1. Transmutation of the long-lived high radiotoxic fission products (^{129}I and ^{99}Tc) into shorter lived species.

2. Production of useful quantities of radioisotopes that are difficult or impossible to produce with conventional means, reactors or cyclotrons.

The above objective can be split into two subcategories: a) Small scale feasibility study which includes physics of photon/neutron production mechanisms, adequacy-check of simulation tools, and experimental verification of calculation methods and b) Scaling up the transmutation setup so that it can be practical for either LLFP transmutation or radioisotope production (or both). The emphasis here is on the former part of the problem.

Accomplishing the first objective is necessary for addressing the second one, which clearly is an engineering and economics problem. The last chapter of this dissertation, Chapter 5, will discuss a possible design of a large-scale transmutation system for one of the fission products, ^{129}I, using the results obtained in this work. In the case of radioisotope production, the results clearly show that useful amounts of activity can be produced by photonuclear methods and scaling up depends on issues of separation chemistry. In summary, the work described in this dissertation aims to address the following topics:

- Study of interactions of radiation with matter
- Study of photon and neutron field production methods
- Computer modeling of single and mixed radiation field production
- Feasibility studies of nuclear waste transmutation and radioisotope production of certain nuclides by simulation and experimentation

Chapter 2

Physics and Formulations

Quantum Electrodynamics (QED) is the formal theory which describes the interactions of electromagnetic radiation with matter [22, 23]. However, owing to the complexity of the problems to be addressed in this study, only a phenomenological approach to the theory will be introduced. Since the very physics of interaction governs each section of the study, from particle creation to radiation detection, and from probability of interaction to final outcome, it is important to take a glimpse at the simplest form of interaction mechanisms and underlying physics.

2.1 Interaction of Electrons with Matter

When an electron penetrates into matter, it interacts with atomic electrons and nuclei present in the material via the electromagnetic force. An electron can lose its energy by different mechanisms, such as elastic and inelastic scattering, ionization, braking radiation (bremsstrahlung), Cherenkov radiation, nuclear reactions, and transition radiations. These interactions produce secondary electrons and photons with continuous or characteristic energies.

2.1.1 Electromagnetic Cascade

Bombarding a target mass with high energy electrons or photons will result in the development of an electron-gamma shower, also known as an electromagnetic cascade. A high energy electron induced cascade develops starting with a high energy electron producing a high energy bremsstrahlung photon. This photon could experience pair-production

and Compton scattering (for high energies atomic processes can be ignored) before it produces more photons and electron-positron pairs by the bremsstrahlung process.

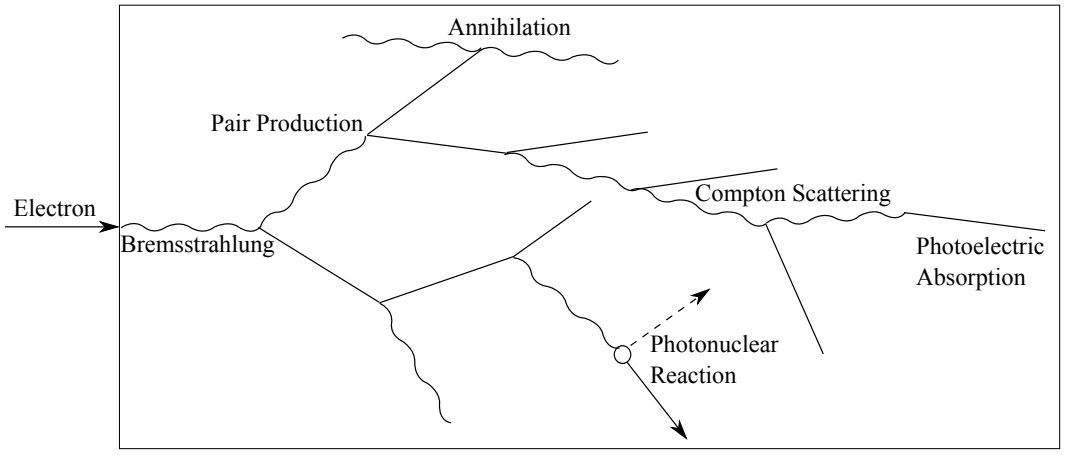

Figure 2.1: Schematic diagram of a high energy electron induced electromagnetic cascade illustrating bremsstrahlung radiation, pair production, annihilation, Compton scattering, photoelectric effect, and photonuclear reaction.

As the process develops, the incident electron energy is shared by more and more low energy shower particles. The number of shower particles rises to its maximum as a function of shower depth and falls off exponentially after the saturation point due to the escape of particles from the mass and dissipative atomic processes. The bremsstrahlung photons are mostly forward directed and their angular distribution is a function of the incident electron energy.

The number of shower particles can be determined in equilibrium by the cascade shower theory. The average behavior of showers cannot be quantified mathematically without certain simplifications and approximations. "Cosmic-Ray Theory" [24] by R. Rossi carries out a full mathematical derivation of shower theory, which states only a few layers of shower depth are needed to reach a maximum production of photons suggesting the use of a thin, high Z material as a photon converter. A thin converter, however, may allow excessive residue electrons to pass through, causing undesirable interactions. Production

of photoneutrons as secondary shower particles needs a thicker target to fully populate photonuclear interactions. A thick material limits the production of photons and the number of pass-through electrons.

In the following sections, a simple form of bremsstrahlung radiation and photoneutron production will be introduced using the classical theory of electrodynamics and the thick target approximation method of the shower theory.

2.1.2 Bremsstrahlung Radiation

Charged particle radiation is fully understood in quantum electrodynamics and the quantum theory of radiation [25]. However, as an intuitive and simple approach, relativistic approximations can be made to the classical electromagnetic radiation theory to describe high energy electron induced bremsstrahlung radiation. A direct consequence of the classical theory of electrodynamics is that a charged particle, when accelerated, radiates an electromagnetic wave. If a charge is accelerated, but is observed in a reference frame where its velocity is small compared to that of light, then in that coordinate frame the acceleration field is [26]

$$\mathbf{E}_a = \frac{e}{c}\left[\frac{\mathbf{n}\times(\mathbf{n}\times\dot{\beta})}{R}\right], \tag{2.1}$$

where $\mathbf{n}$ is a unit vector, $\beta = \mathbf{v}/c$, and R is the radius of the curvature. Thus, the energy flux is given by the Poynting vector

$$\mathbf{S} = \frac{c}{4\pi}\mathbf{E}\times\mathbf{B} = \frac{c}{4\pi}|\mathbf{E}_a|^2\mathbf{n}. \tag{2.2}$$

This means that the power radiated per unit solid angle is

$$\frac{dP}{d\Omega} = \frac{e^2}{4\pi c^3}|\dot{\mathbf{v}}|^2\sin^2\Theta, \tag{2.3}$$

where Θ is the angle between the acceleration and the unit vector. The total radiated power is obtained by integrating Eqn. 2.3 over all solid angles. Thus

$$P = \frac{2e^2}{3c^3}|\dot{\mathbf{v}}|^2 = \frac{2e^2}{3m^2c^3}\left(\dot{\mathbf{p}}\right)^2, \tag{2.4}$$

where **p** is the charged particle momentum.

When an electron is incident on an atom, the Coulomb field of an atomic nucleus causes electron acceleration and bremsstrahlung radiation. The effect is two-fold: one is electron-nucleus radiation (ENR) and the other one is electron-electron radiation (EER). In the ENR process, the atomic electrons screen the Coulomb field of the nucleus as a static charge distribution and the recoil momentum is taken up by the atom as a whole. In the EER process, the atomic electrons act as individual particles and the bremsstrahlung process may also take place in the collision with an atomic electron, which then absorbs the recoil momentum and is ejected.

In the case of ENR, the radiation is dominated by electric dipole radiation, which is determined by the second derivative of the dipole moment. The angular distribution of a non-relativistic radiating dipole (Eqn. 2.3) is only valid for low energy incident electrons. At relativistic energies, the bremsstrahlung angular distribution becomes

$$\frac{dP}{d\Omega} = \frac{e^2\dot{v}^2}{4\pi c^3}\frac{\sin^2\theta}{(1-\beta\cos\theta)^5}. \tag{2.5}$$

As $\beta \to 1$, the angular distribution is tipped forward more and more and increases in magnitude. (Fig. 2.2)

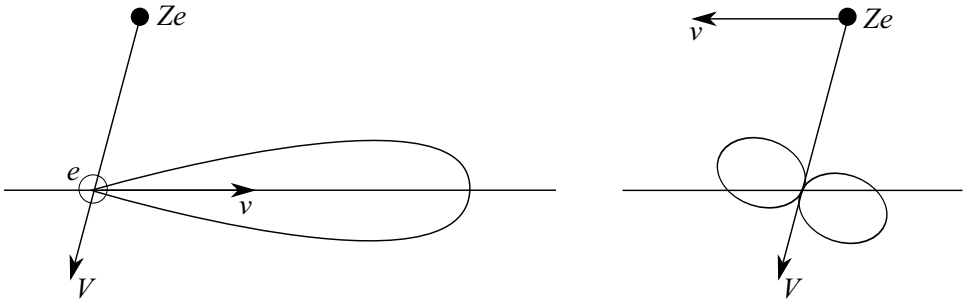

Figure 2.2: Radiation emission during relativistic collisions viewed from the laboratory (nucleus at rest)(left) and the particle frame (incident particle at rest)(right). [26].

In the case of EER, the system has no dipole moment. In the center-of-mass electron-electron radiation system, the total electric dipole moment is initially zero and remains

zero if the recoil due to the photon emission is neglected. Hence, the EER system consists predominantly of electric quadrupole radiation with four lobes in the angular distribution.

ENR is the dominant form of bremsstrahlung radiation due to the pronounced dipole moment radiation and the high probability of interaction with greater charge of the nucleus or atom . Because of its greater charge, the nucleus is more effective at producing deflections of the incident particle than the electron. Consequently, we only consider the radiation emitted in the collision of an electron with a charge of Ze. Thus, the classical radiation cross section is

$$\frac{d\mathcal{X}}{d\omega} = \frac{16}{3}\frac{Z^2e^2}{c}\left(\frac{e^2}{mc^2}\right)\cdot\frac{1}{\beta^2}\cdot\ln\left(\frac{Q_{max}}{Q_{min}}\right), \tag{2.6}$$

where Q is the momentum transfer of the interaction.

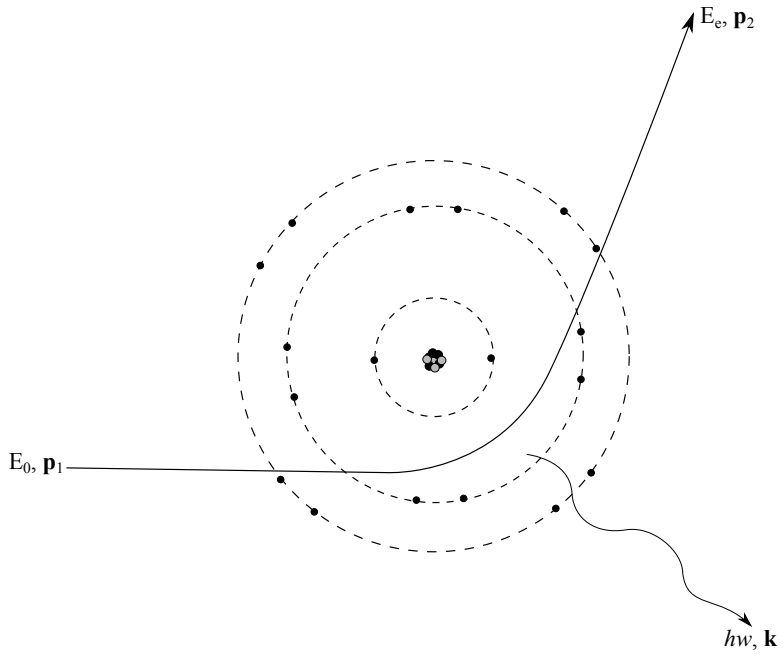

Figure 2.3: A sketch of a charged particle radiation by the Coulomb field of a nucleus.

If we consider an electron with initial kinetic energy (E_0) and momentum ($\mathbf{p}_1$) which is scattered by the Coulomb field of a nucleus or an atom at rest, there will be a certain probability that a photon with energy $\hbar\omega$ and momentum $\mathbf{k}$ is emitted where the electron

makes a transition to a state with energy E_e and momentum $\mathbf{p}_2$ (Fig. 2.3). According to the conservation of energy and momentum,

$$E_e = E_0 - \hbar\omega;\ Q = \sqrt{\mathbf{p}_1 - \mathbf{p}_2 - \mathbf{k}};\ \frac{Q_{max}}{Q_{min}} = \frac{p_1 + p_2}{p_1 - p_2} = \frac{(\sqrt{E_e} + \sqrt{E_e - \hbar\omega})^2}{\hbar\omega}. \quad (2.7)$$

The classical radiation cross section becomes

$$\frac{d\mathcal{X}}{d\omega} = \frac{16}{3}\frac{Z^2e^2}{c}\left(\frac{e^2}{mc^2}\right)\cdot\frac{1}{\beta^2}\cdot\ln\left[\frac{(\sqrt{E_e} + \sqrt{E_e - \hbar\omega})^2}{\hbar\omega}\right], \quad (2.8)$$

which is exactly the quantum-mechanical result in the Born approximation calculated by Bethe and Heitler [27]. The shape of the radiation cross section as a function of frequency is shown in Fig. 2.4.

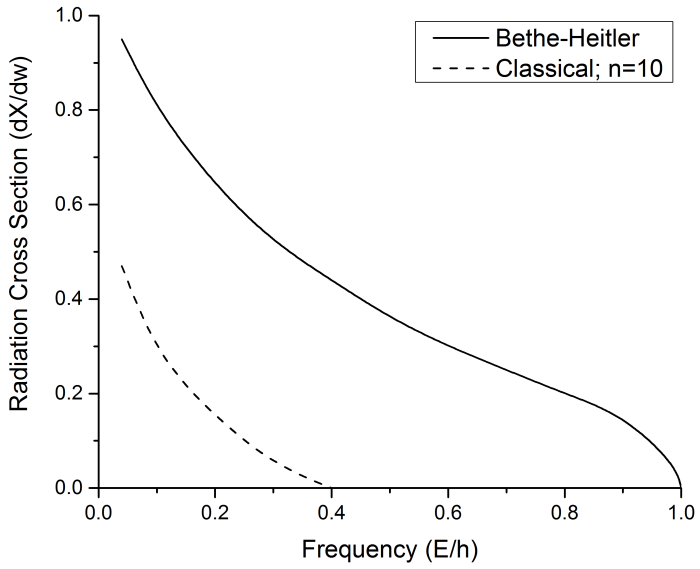

Figure 2.4: Radiation cross section for nonrelativistic Coulomb collisions as a function of frequency in units of the maximum frequency ($E/\hbar$). The classical spectrum is confined to very low frequencies. The curve marked "Bethe-Heitler" is the quantum-mechanical Born approximation result. [26]

Electrons are relativistic when their energy is above a few MeV. Thus, the limits obtained from the conservation of energy calculations must be modified. First, momentum

transfer Q is no longer determined by kinematics. Second, the photon's momentum can no longer be ignored in determining the minimum momentum transfer. With these modifications, the bremsstrahlung radiation cross section becomes

$$\frac{d\mathcal{X}}{d\omega} = \frac{16}{3}\frac{Z^2e^2}{c}\left(\frac{e^2}{mc^2}\right)\cdot\ln\left(\frac{E_0E_e}{mc^2\hbar\omega}\right), \tag{2.9}$$

which is the same as is obtained quantum mechanically in the relativistic limit. The double differential in the radiation cross section for energy radiated per unit frequency interval and per unit solid angle is

$$\frac{d^2\mathcal{X}}{d\omega d\Omega} = \left[\frac{3\gamma}{2\pi}\frac{(1+\gamma^4\theta^4)}{(1+\gamma^2\theta^2)^4}\right]\cdot\frac{d\mathcal{X}}{d\omega}, \tag{2.10}$$

where θ is the angle of emission of the photon and $d\mathcal{X}/d\omega$ is given by Eqn. 2.9.

The above analysis gives only a rough approximation when using a thick photon converter. Comprehensive understanding of bremsstrahlung from electromagnetic radiation requires detailed considerations of all other effects, including screening effects, relativistic energy loss, attenuation, and radiation length of different materials through simulations presented in the next Chapter using Monte Carlo computer modeling, which takes all the effects and mechanisms into consideration.

2.2 Interaction of Photons with Matter

Energetic photons are equally capable of producing an electromagnetic cascade [28] by photoelectric effect, Compton scattering, pair-production, coherent scattering, and photonuclear interactions. Depending on the incident photon energy and nature of the media, different interactions are dominant. Photonuclear reaction is one of the least probable interaction modes. Photonuclear reaction is also a focus of this work which will be introduced in more detail.

2.2.1 Photonuclear Interaction

When a nucleus is bombarded with energetic photons (above few MeV), the absorption

of the photons' energy leads to an intermediate excited state; the excited state of this so-called compound nucleus can then release energy by emitting photons, neutrons or charged particles.

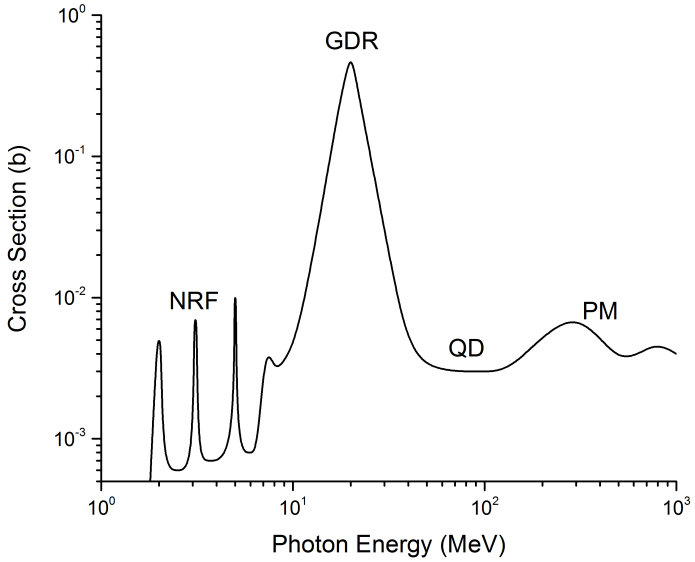

Figure 2.5: Total photo-absorption cross section. Adapted from [2].

1. Nuclear Resonance Fluorescence (NRF): In this energy region, excitation generally occurs at individual nuclear levels, and single-level excitations are observed. Primary emissions are γs with generally small cross sections in the range of nanobarns to microbarns.

2. Giant Dipole Resonance (GDR): In this energy region, photons have enough energy to eject neutrons or protons from the nucleus. Cross sections range from tens to hundreds of millibarns. Primary emissions are protons, neutron, α particles, γs, and fission fragments.

3. Quasi-Deuteron Region (QD): In this energy region, the photon wavelength is smaller than the size of a nucleus, thus it cannot excite the entire nucleus, but can interact with individual neutrons and protons. The cross section ranges from 1 to 10 millibarn.

4. Photo-Meson Production (PM): In this region the wavelength of a photon is comparable to the size of neutrons and protons, which allows for direct interaction with nucleons. This is the energy range where the delta resonance can be induced.

2.2.2 Giant Dipole Resonance

In the energy range of 10 to 30 MeV, the photon has the frequency comparable to the natural frequency of nucleus oscillations and it comes into a resonance with the nucleus. The so-called giant dipole resonance is characterized by a collective vibrational motion of all protons against all neutrons within the nucleus. The most important contribution comes from the dipole mode, hence the name giant dipole resonance.

The giant dipole resonance peak cross section for photonuclear reaction can be explained in semi-classical theory [2]

$$\sigma(E_\gamma) = \sigma_0 \frac{E_\gamma^2(\Gamma/2)^2}{\left(E_\gamma^2 - E_0^2\right)^2 + E_\gamma^2(\Gamma/2)^2}. \tag{2.11}$$

Here σ_0 is the peak cross section, E_0 is the peak resonance energy, and Γ is the full width half maximum (FWHM) for the GDR peak. The width Γ varies between 4 MeV and 8 MeV for medium and heavy nuclei. The peak cross section strongly increases with increasing mass number.

Semi-classical theory of electromagnetic radiation also reveals the empirical expression for the total photo-absorption cross section as [29]:

$$\int \sigma\left(E_\gamma\right) dE = 60(\frac{NZ}{A})\ [\text{MeV} \cdot \text{mbarn}], \tag{2.12}$$

where N is the number of neutrons in the nucleus, Z is the number of protons, and A is the mass number ($A = N + Z$).

The giant dipole resonance is the primary contributor to the total photon absorption cross section; all other vibrational-mode contributions are generally negligible. We can see from Eqn. 2.12 that the integrated cross section increases with increasing atomic number Z of the target nuclei. On the other hand, the peak resonance energy E_0 slowly decreases

with increasing mass number A. E_0 ranges from about 24 MeV in ^{16}O to 14 MeV for ^{238}U [30].

$$E_0 \approx (40A^{-\frac{1}{3}} + 7.5) \text{ MeV}. \tag{2.13}$$

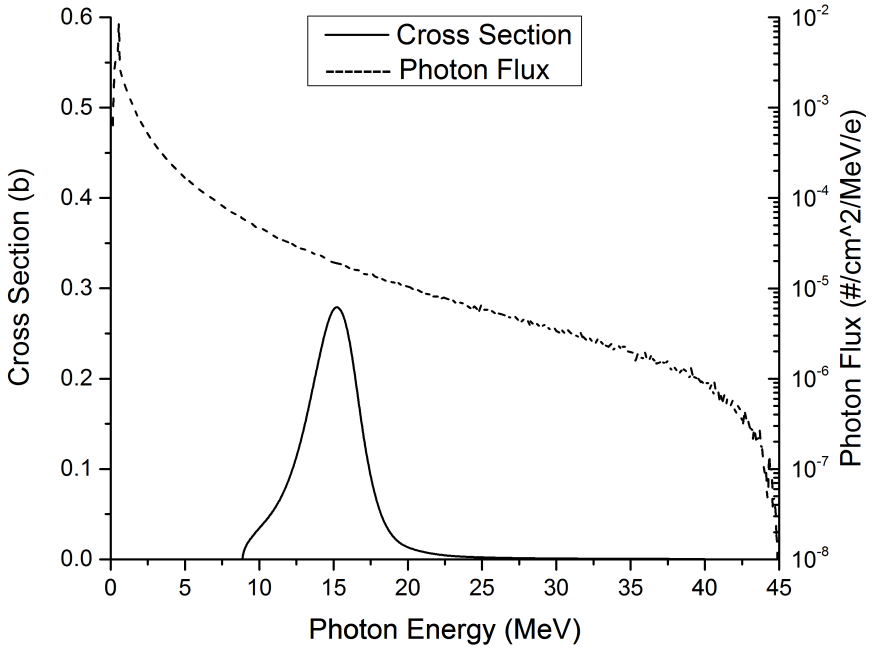

Figure 2.6: Bremsstrahlung spectrum and GDR cross section; Bremsstrahlung photon flux spectrum by a 45 MeV incident electron using MCNPX code (scale on the right); Energy-differential cross section of ^{129}I(γ,n)^{128}I (scale on the left).

Fig. 2.6 shows that the bremsstrahlung energy distribution is continuous up to the endpoint energy and has a characteristic $1/E_\gamma$ falloff. So, high enough energy of the electron beam is necessary to get sufficient photon flux covering the GDR regime. While the (γ, n) reaction is the primary reaction type in the GDR regime, other reactions such as (γ,p), $(\gamma, 2n)$, $(\gamma, 3n)$, (γ, np), and $(\gamma, 2p)$ are also present. However, the threshold energies for $(\gamma, 2n)$ or $(\gamma, 2p)$ reactions are almost twice as high as those of (γ, n) or (γ, p)

reactions, and the peak cross sections for higher order reactions are lower than those of single-nucleon emission reactions. The (γ, n) and (γ, p) reactions have comparable threshold energies due to similar nucleon separation energies. However, typical (γ, n) reaction has a peak cross section about an order of magnitude higher than that of (γ, p) reaction. Therefore, according to the bremsstrahlung energy continuum flux distribution (Fig. 2.6), the most important contribution to the GDR region is the single-neutron or single-proton emission reaction type. The (γ, n) reaction threshold slightly decreases with increasing atomic number and its effective cross section increases with increasing atomic number as shown by Eqn. 2.12.

2.2.3 Photoneutron Production

Photoneutron yield can be estimated using the thick target approximation method, where the target is treated as infinitely long and the electron energy is assumed to be more than 30 MeV so atomic processes can be neglected. The track length of a photon in a target can be found as [31]

$$L = 0.572 \ \frac{X}{\rho} \frac{E_e}{E_\gamma^2}, \tag{2.14}$$

where X is the radiation length (g/cm^2), ρ is the density (g/cm^3) of the target material, and E_e is the energy of electron beam. Since E_γ varies only slightly over the main contribution of GDR cross section (e. g., 12 to 17 MeV for ^{129}I(γ,n)^{128}I in Fig. 2.6), it can be replaced by the peak resonance energy E_0 (e. g., 15 MeV in Fig. 2.6) as a constant. In terms of photon tracking length and photoneutron cross-section by the GDR, the photoneutron yield is given by:

$$Y = 0.572 \frac{\mathcal{N}_A X E_e}{A E_0^2} \int \sigma\left(E_\gamma\right) dE. \tag{2.15}$$

Thus, approximate numerical results of photoneutron yield can be obtained by Eqns. 2.12, 2.13, and 2.15 assuming that a high energy monochromatic electron beam strikes a high Z thick target. For example, a 10 kW electron linac (i.e. JACK linac at the IAC) can

generate 10^{13} photoneutrons per second using a thick tungsten converter when operating at its highest power 10 kW and 40 MeV (Chapter 5).

Although most produced photoneutrons have energies less than a few MeV, photoneutrons will have a continuous evaporation type flux spectrum similar to a nuclear fission neutron spectrum where the highest photoneutron energy is below the maximum energy of the photon, if the effect of nuclei recoil is ignored.

More detailed simulations were carried out using Monte Carlo particle transport tools since it can describe the real physics interactions much more accurately without rough approximations. Jon Handrickson from LANL once said "All the physics known to date is included in the Monte Carlo simulation codes" [32].

2.3 Interaction of Neutrons with Matter

Unlike electrons or photons, neutrons undergo extremely weak electromagnetic interactions. A neutron interacts with matter mainly by scattering and/or nuclear absorption.

2.3.1 Scattering

Scattering events can be subdivided into elastic (n, n) and inelastic scattering (n, n'). In the elastic scattering process, the total kinetic energy of the neutron and nucleus is unchanged. During the interaction, a fraction of the neutron's kinetic energy is transferred to the nucleus. For a neutron of kinetic energy E_0 encountering a nucleus of atomic weight A, the average energy loss is

$$E_{loss} = \frac{2E_0A}{(A+1)^2}. \tag{2.16}$$

Thus, in order to reduce the neutron energy from initial energy of E_0 to E_n, where

$$E_n = E_0 \left[\frac{A^2+1}{(A+1)^2}\right]^n, \tag{2.17}$$

it requires n collisions where

$$n = \frac{\log(E_n/E_0)}{\log[(A^2+1)/(A+1)^2]}. \tag{2.18}$$

Inelastic scattering is similar to elastic scattering except that the nucleus undergoes an internal rearrangement into an excited state from which it eventually releases radiation. Both elastic and inelastic scattering processes are the major means of neutron energy moderation (Table 2.1).

Table 2.1: Average number of collisions required to reduce a neutron's energy from 2 MeV to 0.025 eV by scattering for different materials.

Element	Atomic Weight (A)	Number of Collision (n)
Hydrogen	1	27
Deuterium	2	31
Helium	4	48
Beryllium	9	92
Carbon	12	119
Uranium	238	2175

2.3.2 Nuclear Absorption

Instead of being scattered by a nucleus, a neutron may be absorbed or captured. A variety of interactions may follow such as radioactive capture (n, γ), charged or neutral particle emission $((n, p),\ (n, 2n))$, and fission (n, f). Neutron absorption reactions are the basis for the many neutron detection techniques, since lack of an electric charge of a neutron makes direct detection difficult.

Scattering should be the main interaction process when neutron energy moderation is the main goal. For instance, although hydrogen needs fewer collisions to moderate neutrons, lower absorption cross section of deuterium makes it a better moderator.

Because of this very nature of neutron interaction, thermal neutrons yield a higher cross section to induce absorption reactions. In most cases, at low energies, the elastic cross section is nearly constant, whereas the inelastic scattering cross section and absorption cross sections are proportional to the reciprocal of the neutron's speed $(1/V)$. For

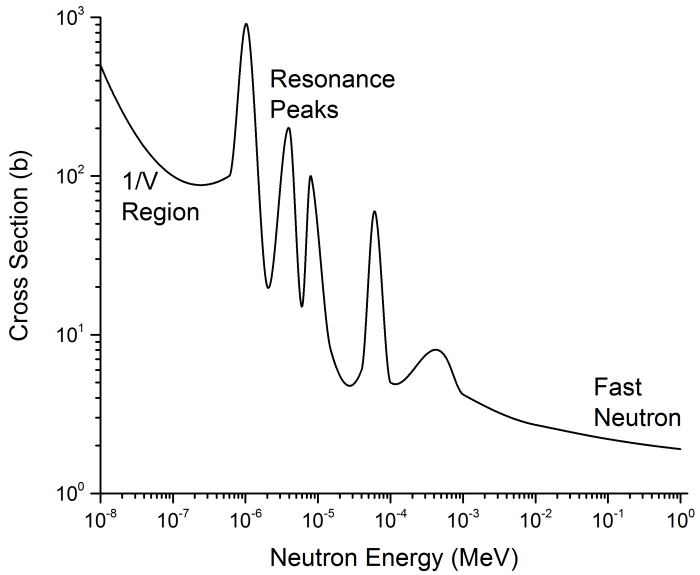

Figure 2.7: Total neutron absorption cross section. [33]

heavy nuclei, large and narrow resonances appear for the neutron energies in the eV range. For light nuclei, resonances appear only in the MeV region and are broad and relatively small (Fig. 2.7). Some exceptions exist in ^{1}H and ^{2}H where there are no resonances at all and in nuclei with "magic" numbers of protons or neutrons where the behavior may be similar to that of light nuclei despite the actual atomic weight.

2.4 Nuclear Radiation and Decay

Photonuclear reaction of GDR-photons or nuclear absorption of neutrons can produce a proton or a neutron rich isotope of the interrogated element. In most cases, the isotope is unstable and this excited nuclide will cascade down to its ground state emitting several gamma rays each having a characteristic energy ranging from 100 keV to several MeV. Characteristic gamma energies can be used to fingerprint the target nuclide and radioactivity analysis of product nuclide can reveal information about nuclear reaction.

2.4.1 Nuclear Decay

Nuclear decays are the result of releasing excessive energies from a nucleus so that a more stable state, or stable species can be formed. Energies released can be in the form of a particle or a quanta. There are three primary decay types: α, β, and γ decays. In α and β-decay processes, an unstable nucleus emits an α or a β particle as it tries to become a more stable nucleus. In γ-decay processes, an excited state decays toward the ground state without changing the nuclear species.

α decay

In this process, a tightly bound ^{4}He nucleus will be emitted from a larger nucleus. The number of protons and neutrons is conserved in the initial and final state of the nuclei.

β decay

A proton or neutron rich nucleus can directly convert a proton into a neutron, or a neutron into a proton, by releasing excessive energy. This process can occur in three possible ways, each of which must involve a charged particle to conserve electric charge. The first process is β^- decay and involves the creation and emission of an electron. The second process is β^+ decay or positron decay. In the third process, an atomic electron acts as the conversion of a proton to a neutron.

γ decay

In the γ decay process, an exited state decays to a lower excited state (or possibly the ground state) by the emission of a photon with an energy equal to the difference in energy between the nuclear states (recoil energy of the nucleus is usually negligible)(Fig. 2.8). The γ decay is usually followed by α and β decay processes since these processes lead to excited states of the daughter nucleus.

Although some nuclei may decay only through a single process, more often decay processes involve several competing decaying modes of α, β and γ. The branching ratio describes relative intensities of the competing modes. For instance, a ^{27}Mg nucleus decays

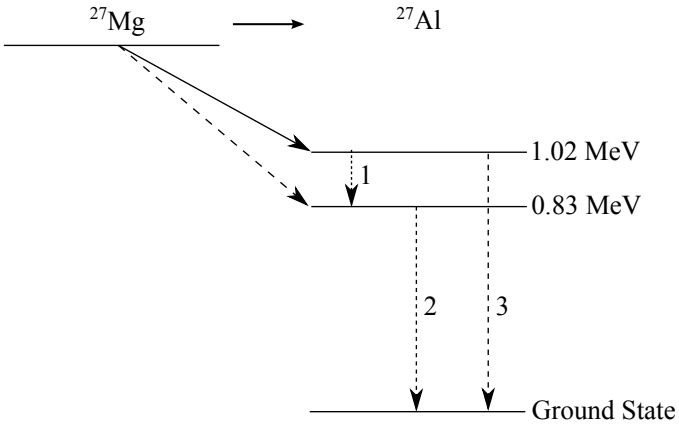

Figure 2.8: Schematic energy level diagram. Transition 1 results in a gamma of 170.68 keV with an emission probability of 0.8%; Transition 2 results in a gamma of 843.74 keV with an emission probability of 71.8%; Transition 3 results in a gamma of 1014.42 keV with an emission probability of 28%.

through β^- with 100% branching ratio,

$$^{27}_{12}Mg \longrightarrow {}^{27}_{12}Al + \beta^- + \nu_e \tag{2.19}$$

producing a stable ^{27}Al nucleus; energy will be emitted by several gammas whose energies are determined by transitional energy difference of nuclear states (Fig. 2.8).

2.4.2 Reaction Yield and Radioactivity

Reaction yield is the transition rate from the target nuclide to the product nuclide; radioactivity is a quantity of the decay rate of the product nuclide. However, these two quantities are related. We start with the number of target nuclei in the target

$$N_o = \frac{\mathcal{A}M\mathcal{N}_A}{A_r}, \tag{2.20}$$

where M is the mass of the sample, $\mathcal{A}$ is the natural abundance of the target isotope, $\mathcal{N}_A$ is the Avogadro's constant, and A_r is the relative atomic mass.

When the target is irradiated with high-energy photons or neutrons, the target nuclide will be activated with a characteristic reaction rate of η, which is the transition rate of target nuclides to radioactive nuclides. η is a function of the photon or neutron flux density $\Phi(E)$ and the reaction cross section $\sigma(E)$,

$$\eta = \int_{E_{th}}^{E_{\max}} \Phi(E) \cdot \sigma(E)\, dE. \tag{2.21}$$

Thus, the nuclear reaction yield can be written as [2]

$$Y = N_o \cdot \int_{E_{th}}^{E_{\max}} \Phi(E) \cdot \sigma(E)\, dE. \tag{2.22}$$

The production rate of radioactive nuclides is equal to the transition rate of the target nuclides, i.e. the number of radioactive nuclides are the number of produced radioactive nuclides from target nuclides less the decayed nuclides. Solving for the number of product nuclides in the target, one obtains

$$N(t) = \frac{Y}{\lambda}\left(1 - e^{-\lambda t}\right), \tag{2.23}$$

where λ is the decay constant of the radioactive nuclide.

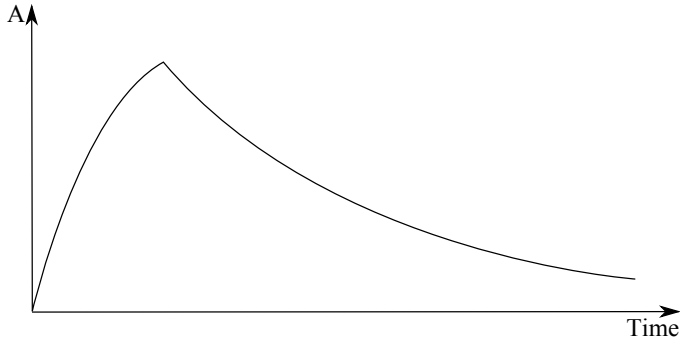

Figure 2.9: Activity curve depicting a rise due to a continuous irradiation and a fall due to radioactive decay.

During the irradiation of the sample for a time period (T_i), constant production of radioactive nuclides will give rise to the activity curve. After the irradiation stops, the

radioactive nuclide will decay through different decay modes. The typical radioactive nuclide activity curve is shown in Fig. 2.9. When the irradiation stops, no more radioactive nuclides will be produced. The activity of a radioactive nuclide after T_i can readily be derived as:

$$A(t)|_{t>T_i} = Y(1 - e^{-\lambda T_i})e^{-\lambda t}. \tag{2.24}$$

Rewriting Eqn. 2.24 using Eqn. 2.22 and inserting the original number of target nuclides N_o, one obtains a general equation of activity:

$$A(t)|_{t>T_i} = \frac{M\mathcal{A}\mathcal{N}_A}{A_r}(1 - e^{-\lambda T_i})(e^{-\lambda t}) \int_{E_{th}}^{E_{\max}} \Phi\left(E\right) \cdot \sigma\left(E\right) dE. \tag{2.25}$$

To detect the photon emissions, gamma spectrometry is commonly used. Emitted gamma rays from the radioactive nuclide produce electric signals (pulses) in the detector crystal. Intensity of the signal is translated into gamma ray energy and re-occurrence of the same-intensity signal is translated into the number of counts (Fig. 2.10).

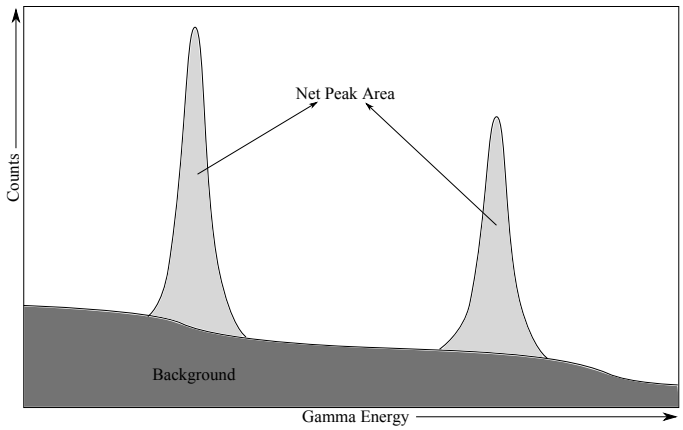

Figure 2.10: A spectrum with two gamma peaks showing background counts and the total counts under the peak. Adapted from [2].

The count rate obtained through a gamma spectrometer is:

$$R = A \times \varepsilon \times \mathcal{P}_\gamma, \tag{2.26}$$

where A is the activity of the nuclide, ε is the counting efficiency of the detector which is a function of energy and solid angle, and $\mathcal{P}_\gamma$ is the emission probability of the γ-radiation.

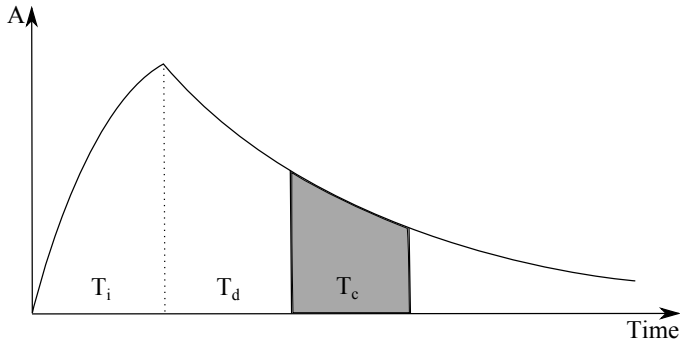

Figure 2.11: Radioactivity curve showing irradiation, decay, and counting times.

After the irradiation, the target "cools" for a period of T_d, after which it is counted for a period of T_c with a high purity germanium (HPGe) detector (Fig. 2.11). The net peak area (Fig. 2.10) can be obtained by integrating over the time period,

$$P = \int_{T_c} Re^{-\lambda t} dt = \int_{T_c} \varepsilon \mathcal{P}_\gamma e^{-\lambda t} A(t)|_{t>T_i} dt, \tag{2.27}$$

and the solution to the above equation is:

$$P = \frac{\varepsilon \mathcal{P}_\gamma A(T_c)}{\lambda}(1 - e^{-\lambda T_c}). \tag{2.28}$$

Combining Eqns. 2.25, 2.26, and 2.28, one obtains a general equation of the peak area:

$$P(T_i, T_d, T_c) = \frac{M\mathcal{A}\mathcal{N}_A \varepsilon \mathcal{P}_\gamma}{A_r \lambda}(1 - e^{-\lambda T_i})e^{-\lambda T_d}(1 - e^{-\lambda T_c}) \int_{E_{th}}^{E_{\max}} \Phi(E)\,\sigma(E)\,dE. \tag{2.29}$$

The radioactivity of product nuclide expressed by the peak area is:

$$A|_{(t=T_i)} = \frac{P\lambda}{\varepsilon \mathcal{P}_\gamma}(e^{-\lambda T_d})(1 - e^{-\lambda T_c}). \tag{2.30}$$

Radioactive decay is the direct outcome of an excitation of the nuclear energy levels. Hence, the radioactivity is often used to interpret the details of undergoing physics and interaction mechanisms.

Chapter 3

Computer Modeling

Complicated physical processes require detailed calculations in order to comprehend the collective effects. Computers can aid us in modeling the real world. One of the most common modeling techniques in physics is the Monte Carlo method, which follows the history of individual particles and averages the behavior that inferred from the collective effect of many particles. The probability distributions governing these events are statistically sampled to describe the total phenomenon such that the average behavior of the particles can be realistically quantified.

3.1 Monte Carlo N-Particle eXtended (MCNPX)

MCNPX [34] is a computer modeling tool for nuclear processes which was developed at Los Alamos National Laboratory (LANL). It was initially designed for the simulation of nuclear fission processes, but has been expanded to have the capability to simulate particle interactions involving neutrons, photons, electrons, and 31 other particles at nearly all physically realistic energies (Appendix B).

All current evaluated data and physics models have been included in the MCNPX code, so that the simulation of photonuclear processes is well described [35]. Photonuclear cross-sections are available for major isotopes used in structural design, shielding, activation analysis, fission, and transmutation. Neutron physics is also well defined in MCNPX. Continuous energy neutron data can be used for modeling neutron interaction and transport. Neutron histories in user defined geometries are tracked from their creation by using evaluated cross section data libraries for elastic scattering, inelastic scattering

and absorption on nuclei present in the specified materials.

Monte Carlo simulation of radiation transport involves source characterization, target material and geometry specifications, physics process management and output-tallies of the physical quantities of interest (Appendix C).

Several types of tallies were used in this work [32]:

- F2 tally. Particle flux averaged over a surface:

$$F2 = \frac{1}{A}\int_A\int_E\int_\Omega \Phi(r_s, E, \Omega)\ dAdEd\Omega, \tag{3.1}$$

  where A is the surface area (cm^2),Φ is the particle flux (particles/cm^2), r_s is the particle position (cm), and E is the particle energy (MeV). The unit of this tally is "number of particles per cm^2".

- F4 tally. Particle flux averaged over a cell:

$$F4 = \frac{1}{V}\int_V\int_E\int_\Omega \Phi(r_s, E, \Omega)\ dVdEd\Omega, \tag{3.2}$$

  where V is the cell volume (cm^3). This type of estimator is used mainly because the average number of photons in a cell is of particular interest to estimate the net yield of nuclear interaction. The unit of this tally is "number of particles per cm^2".

- F6 tally. Energy deposition averaged over a cell:

$$F6 = \frac{\rho_a}{\rho}\int \Phi H\sigma_t dE; \quad F6 = \frac{1}{m}\left(\Sigma E_{ion} + \Sigma E_{recoil} + \Sigma E_{kinetic}\right), \tag{3.3}$$

  where ρ_a is the atomic density (atoms/barn·cm), ρ is the density of the material (g/cm^3), σ_t total cross section (barn), and H is the heating number (MeV/collision). This type of estimator is used to estimate the energy deposition in a cell volume. The unit of this tally is "MeV per gram".

- FM tally multiplier card. The FM card is used to calculate any quantity of the form

$$FM = C \cdot \int \Phi(E) \cdot R(E)dE, \tag{3.4}$$

where $\Phi(E)$ is the energy-dependent fluence (particle/cm^2), $R(E)$ is an energy-dependent function (such as reaction cross section), and C is a constant that can be used for normalization. FM tally can be used to calculate reaction yield or radioactivity when the nuclear reaction cross section is used for $R(E)$ function. Each reaction cross section has a designated reaction number, so one can find yield of different isotopes using different reactions.

To estimate nuclear reaction yields or radioactivity after a certain exposure time, a normalization constant C needs to be calculated so that the FM card results in nuclear reaction rate (number of nuclear reactions per volume per second):

$$C_r = N_i \cdot \frac{I}{1.6 \times 10^{-19}} \cdot (1 \times 10^{-24}), \tag{3.5}$$

where N_i is the total number of parent isotope in the cell, I is the average electron beam current in Ampere, and a correction term of (1×10^{-24}) comes from the cross section unit conversion from mbarns to cm^2. When normalization constant C_r is used in FM card, the result is given as the number of reactions per second. When a $C = -1$ is used, however, MCNPX takes C as the atomic density of the material in the cell. When using the FM card, results of the reaction rate is defined in "number of reactions per cm^3".

To estimate radioactivity of the product isotope after a certain time of irradiation, the normalization constant should be

$$C_a = N_i \cdot \frac{I}{1.6 \times 10^{-19}} \cdot (1 - e^{-\lambda T_i}) \cdot (1 \times 10^{-24}) \cdot (2.7 \times 10^{-5}), \tag{3.6}$$

where λ is the radioactive decay constant of the product isotope, T_i is the irradiation time, and the term of (2.7×10^{-5}) comes from conversion of becquerel (Bq) to microcurie (μCi).

- Mesh tally. The mesh tally is a method of graphically displaying particle flux, dose, or other quantities on a Cartesian, cylindrical, or spherical grid overlaid on top of the standard problem geometry.

Using the above tallies, one can obtain particle fluxes, energy deposition, nuclear reaction rates, and isotope yields. It should be noted that all MCNPX tally results are normalized to be "per source particle". Therefore, the results always need to be renormalized such that all quantities are calculated as "per mA" or "per kW".

MCNPX has a built-in statistical analysis tool to ensure the reliability of the results. Each simulation result should be examined carefully with these statistical checks. Variance reduction techniques are often used to get converged results in a shorter amount of computer time. DXTRAN spheres, weight cutoff, energy splitting and Russian roulette, source biasing, time and energy cutoff, and weight window generators are some examples of different variance reduction techniques used in this work.

3.2 Photon Production and Optimization

Photon field production depends on numerous factors including incident beam parameters, converter type and shape, and other operational and engineering constraints. It should be noted that optimized design does not correspond to the maximum number of photons produced by the converter, but rather to the maximum number of photons that induce nuclear reactions within the target material.

3.2.1 Electron Beam Quality

Electron energy, energy spread, beam size, beam emittance, and average beam current are vitally important for the tuning of a photon radiation field. However, it is safe to assume that the effects of beam divergence and beam emittance are negligible if the electron beam energy is in the range from tens to a few hundred MeV. Ultimately, the energy distribution of a photon field is determined by the electron energy (Fig. 3.1). Different electron energies can be selected in order to suppress or populate a certain nuclear reaction.

Energy spread can cause changes in the photon flux distribution. For most electron

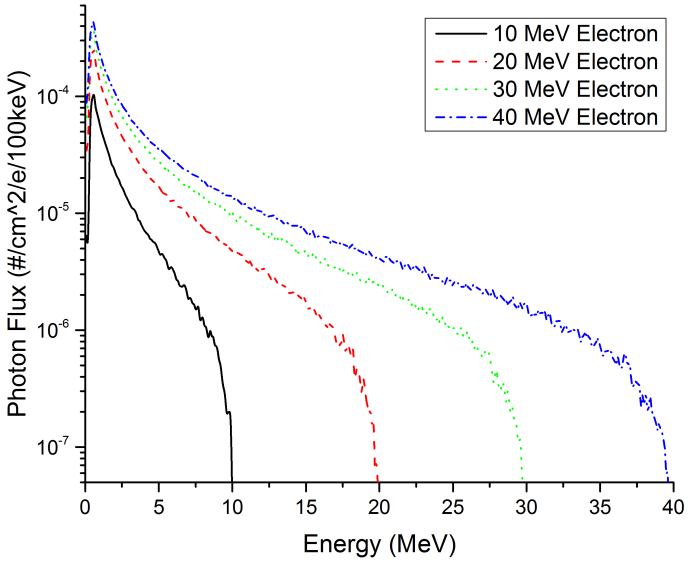

Figure 3.1: MCNPX photon flux spectrum created by different energy electrons incident on a 0.35 cm thick W converter.

linacs, energy distribution closely resembles a Gaussian function. A typical energy spread (FWHM) for a conventional copper electron linac is up to 15% (Appendix B). Energy spread of the L-band 44-MeV linac (housed at the IAC) for a 40 MeV peak energy is about 6 MeV (Fig. 3.2). MCNPX simulations were carried out to investigate the effect of energy spread from 1 to 10 MeV for a nominally 40 MeV beam. Fig. 3.2 shows the results of these simulations. It can be seen that the bremsstrahlung curves slightly differ. However, the integral number of the GDR-photons remains the same and the transmutation rate will not be affected by such a spread of the electron beam energy.

Another set of simulations was carried out in order to compare the photon flux distributions for different electron beam sizes (diameters). As it turns out, the beam size difference will not change the total number of GDR-photons produced as long as the beam size does not exceed the size of the converter. However, it will change the spacial distribution of the photons (Fig. 3.3). This is important when different photon field sizes are

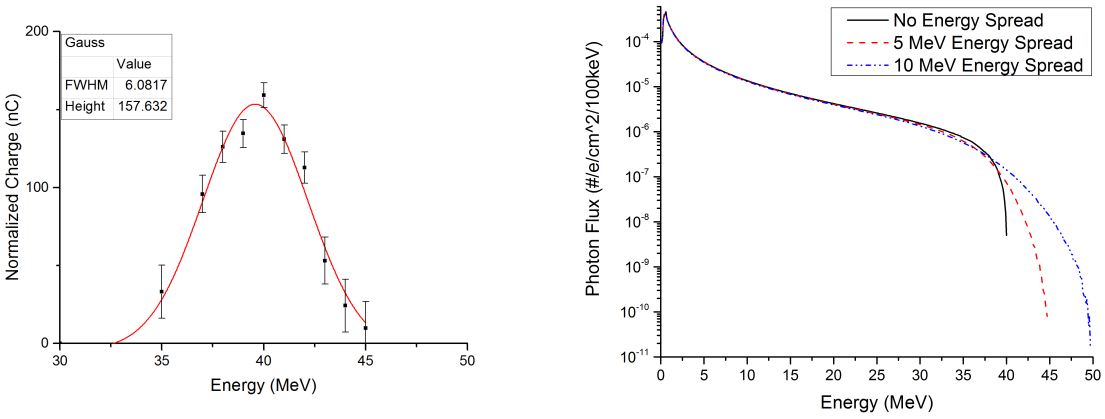

Figure 3.2: Energy spread of the L-band linac at the IAC (left) [36]; MCNPX photon flux generated by electron beams with different energy spread (right).

desired or when regional heat transfer needs to be minimized . A uniformly distributed transverse-profile of photon radiation field can be obtained by an electron beam with a larger beam size.

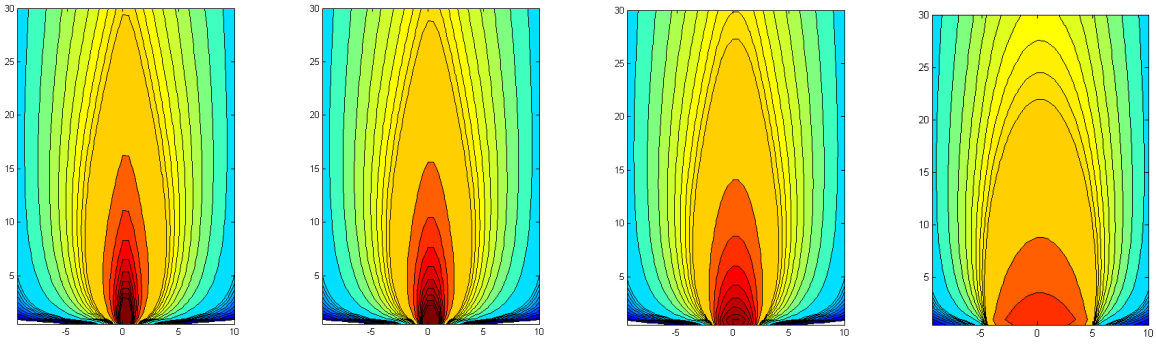

Figure 3.3: MCNPX photon flux distribution from a 40 MeV electron incident on a 0.35 cm thick W converter (radius is 5 cm). Electron beam radii are 0.5, 1, 2, and 5 cm from left to right. Mesh size is 20 cm by 30 cm.

3.2.2 Converter Type and Thickness

As pointed out in Chapter 2, the bremsstrahlung radiation cross section is proportional to Z^2 of the converter material when using thin target approximation. Therefore, a high Z material should be used for an efficient production of photons. The cost of the material, the intensity of residual radioactivity, and the engineering and handling properties are equally as important in determining an optimal converter material. At the IAC, pure W or W-Cu alloy materials are mainly used for the photon field production. MCNPX simulations also confirm that W is one of the best materials for photon production due to its high atomic number and high atomic density.

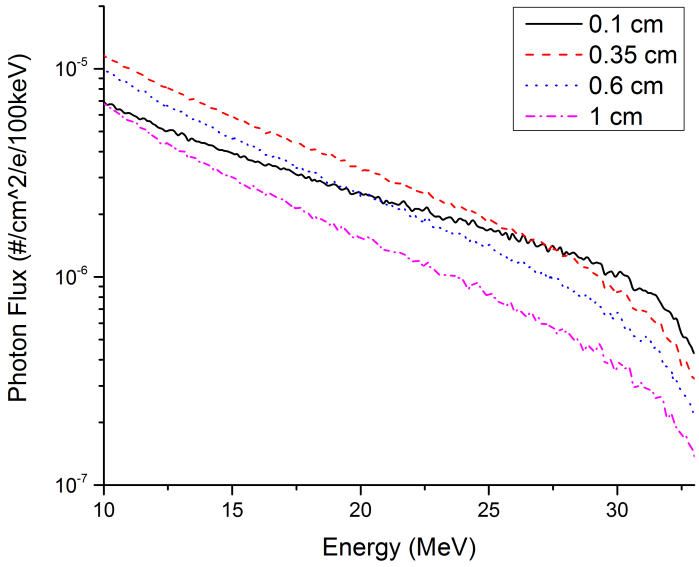

Figure 3.4: MCNPX GDR-photon spectrum created by a 40 MeV electron incident on a 0.1, 0.35, 0.6, and 1 cm thick W converter.

Once the thickness of the target becomes significant, photons start attenuating and the photon flux intensity decreases as thickness increases. Furthermore, the highest photon flux can be found by optimizing the converter thickness. The radiation length is an important parameter in estimating optimum converter thickness for photon production.

Radiation length is the distance (cm) traveled by an electron after which it loses $1/e$ of its initial energy,

$$X = \frac{714.6}{Z(Z+1)} \cdot \frac{1}{\ln\frac{287}{\sqrt{Z}}}. \tag{3.7}$$

The thickness that corresponds to one radiation length of pure tungsten is 0.35 cm, which is confirmed by the MCNPX simulations shown in Fig. 3.4. Although a 0.1 cm thick converter generates more photons above 27 MeV, the integrated number of GDR-photons are greater with a 0.35 cm thick converter. This result aligns with the theoretical calculations described in Chapter 2 using the cascade shower theory.

3.2.3 High Power Operations

When operating under high power, a heat removal scheme is necessary. For example, if a 0.35 cm thick tungsten plate is used as a photon converter, according to MCNPX calculations, about 60% of the incident beam power is deposited into the converter. Heat capacity and melting point of tungsten is $C = 24.27 J/(mol \cdot K)$ and $T_{melt} = 3422\,^{\circ}\text{C}$. With no heat removal, this converter can only last for

$$t = \frac{\Delta T \times C \times m}{P} = \frac{3402(K) \times 24.27(\frac{J}{mol \cdot K}) \times 0.946(mol)}{1000 \times 0.6(W)} = 130 \text{ [s]}, \tag{3.8}$$

assuming an electron beam with beam power of 1 kW incident on a 5.08 cm× 5.08 cm× 0.35 cm tungsten plate. This means that only 2 minutes of irradiation can be done with this setup for 1 kW beam power before the converter melts.

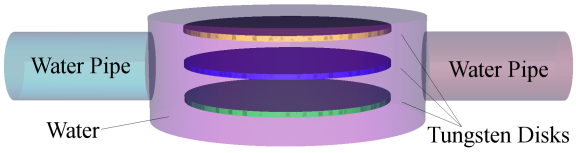

Figure 3.5: Three disk converter design for high power operations.

In order to remove heat efficiently during irradiation, the surface area of the converter needs to be increased and a liquid (or gas) flow needs to be used to remove heat by

conduction. The design we used in this work consists of three tungsten disks (their total thickness equals 0.45 cm) surrounded by flowing water coolant (Fig. 3.5). The conduction process will transfer most of the heat into the water until an equilibrium is established. According to the MCNPX calculations, this particular setup loses about 5% of the photon flux, compared to that of a 0.35 cm thick converter, due to the beam loss through the water.

Advanced liquid metal or alloy converters can be used for even higher power operations where water cooling is not adequate [37, 38]. Commonly used materials are liquid metals and alloys with high thermal conductivity which removes the heat more effectively. They also have higher boiling points than water which allows the converter to operate at higher temperatures.

Table 3.1: Material properties of Hg, LBE, and Pb.

Metal	Melting Point (°C)	Boiling Point (°C)	Thermal Expansivity (1/K)
Hg	-40	350	1.8E-4
LBE	125	1640	1.2E-4
Pb	328	2016	1E-4

Several materials are often considered for this purpose: mercury (Hg), liquid lead (Pb), and lead-bismuth eutectic (LBE). These materials are favorable, not only because of their good thermal-hydraulic properties (Table 3.1), but also due to their high bremsstrahlung production efficiency. MCNPX simulations show that these converters produce similar photon flux distributions as that of a tungsten converter (Appendix B).

3.3 Neutron Production and Optimization

In this work, neutron production was achieved purely by photonuclear interactions of GDR-photons with target nuclei. Photoneutron production is governed by the neutron knockout threshold energy and the photoneutron cross section. On one hand, the energy

of the photons must exceed the threshold energy in order to release a neutron out of a nuclide. On the other hand, the reaction cross section should be high enough to generate a significant number of neutrons in order to form an intense neutron source.

3.3.1 Converter Type and Geometry Design

In general, neutron knockout threshold energy decreases with increasing Z, while photoneutron production peak cross section increases with increasing Z. Therefore, high Z materials are more efficient neutron converters. However, there are some isotopes that are capable of producing significant neutron yields at low energies. Table 3.2 shows a list of isotopes with their neutron knockout threshold energies and peak photoneutron cross section values.

Table 3.2: Threshold energies and peak cross section values of photoneutron production of ^{2}H, Be, Cu, and W nuclides.

Isotopes	Threshold Energy (MeV)	Peak Cross Section (mb)
^{2}H	2.22	2.5
^{9}Be	1.67	5
^{63}Cu	10.85	80
^{65}Cu	9.91	90
^{180}W	8.41	415
^{182}W	8.07	475
^{183}W	6.19	500
^{184}W	7.41	585
^{186}W	7.19	650

To find an optimum material to be used as a neutron converter, a set of MCNPX simulations was done using heavy water, beryllium, copper, and tungsten. The total neutron flux was calculated using different thicknesses of the tabulated materials. A 0.35 cm tungsten photon converter was used followed by a neutron converter of the selected material. By varying the thickness of the neutron converter, an optimum thickness was

found for each material. The MCNPX results show, as expected, that for a 40 MeV electron beam tungsten yields the highest neutron flux followed by copper, beryllium and heavy water. With decreasing Z, the results show that the optimum thickness increases slightly due to a decreasing peak cross section value. To be used as a neutron converter, optimum tungsten thickness is around 2 to 5 cm, while the optimum thickness of beryllium is around 10 cm (Fig. 3.6). These results align with the thick target approximation calculations in Chapter 2 and with other photoneutron production studies [39–42].

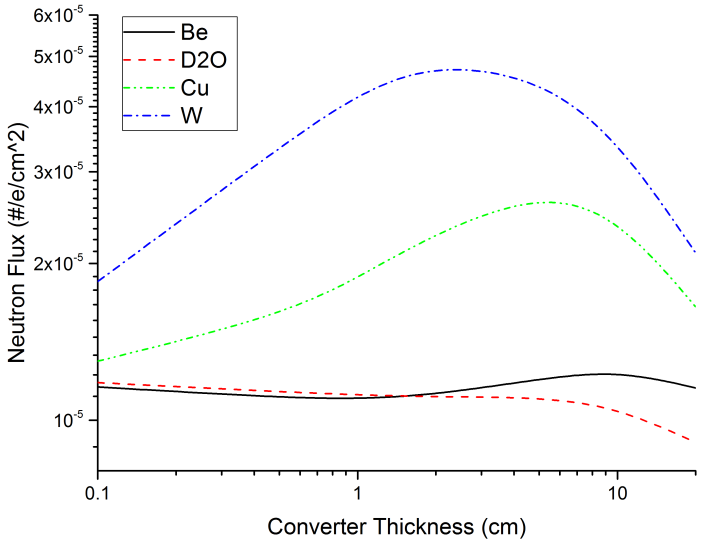

Figure 3.6: MCNPX neutron flux generated in different materials as a function of their thicknesses. A 40 MeV electron beam is incident on a 0.35 cm tungsten followed by a neutron converter. The results are subject to a maximum of 5% uncertainty.

In order to make maximum use of photons and electrons of all energies, and to minimize the engineering complexity and local heat deposition, a single converter can be used for neutron production by direct incident electrons.

Due to its high neutron production efficiency, tungsten serves as the best neutron converter among the materials listed in Table 3.2 for a 40 MeV electron beam. However, only GDR-photons are being utilized in this photoneutron production scheme (Fig. 3.7).

Note that more than 80% of all the bremsstrahlung photons generated by a 40 MeV electron are low energy photons (<10 MeV), and do not contribute to neutron production.

Making use of the low energy photons can increase neutron production. Table 3.2 shows that beryllium and deuterium are the best candidates for this purpose with threshold energies of 1.67 and 2 MeV, respectively. To examine the possible increase in neutron flux that might be obtained by a compound material, we considered tungsten alloyed with beryllium of different weight fractions (Table 3.3).

Table 3.3: Beryllium and tungsten weight fraction and their alloy densities.

Weigh Fraction (M_{Be}/M_W)	0.001	0.01	0.1	0.2	0.5	1	2	5	10
Alloy Density (g/cm^3)	19.07	17.61	10.38	7.50	4.66	3.38	2.65	2.18	2.02

Using different weight fractions and respective densities, numerous MCNPX simulations were performed to find an optimum combination. Although low energy photons can knock out neutrons from Be nuclei, a higher weight fraction of Be/W tends to lower the overall bremsstrahlung production because of a lower net Z value.

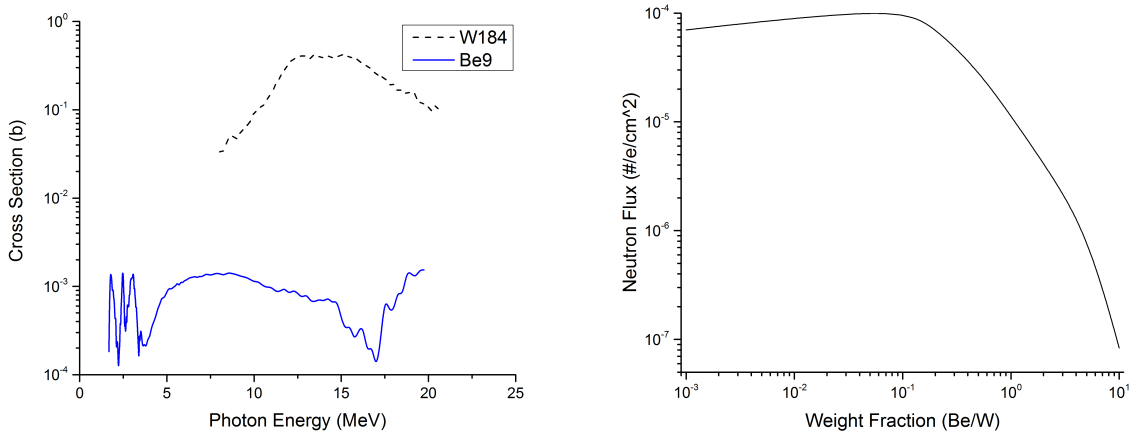

Figure 3.7: The (γ,n) reaction cross sections for ^{9}Be and ^{184}W (left); MCNPX photoneutron flux created by an Be-W alloy converter with different weight fractions (right).

Fig. 3.7 shows that a weight fraction of 0.1 yields the highest neutron production for a 40 MeV incident electron beam. A higher weight fraction of Be dampers neutron production. An alloy of this kind lacks a real practicality for high energy electron induced (> 15 MeV) photoneutron production. Therefore, high purity tungsten remains the best choice for most applications where an intense neutron field is needed. However, for incident electron energy below 15 MeV, a Be-W alloy converter with an optimum weight-ratio can significantly increase neutron production [43].

3.3.2 Neutron Moderation and Reflection

As briefly mentioned in Chapter 2, thermal neutrons have higher absorption probabilities as they spend "longer time" near the surrounding nuclei. Typically, thermal (0.025 eV) or even cold neutrons (< 0.025 eV) can have cross section values of a few thousand barns with many materials, which makes neutron moderation extremely useful to improve the transmutation rate.

High neutron scattering cross section is a must for a good moderator. Moderation power and moderation ratio are often used to select a practical moderator. Moderation power is characterized by the average neutron energy loss per unit distance of travel in the moderator; moderation ratio is characterized by the ratio of moderation power and absorption cross section. A material with high moderation power might be useless as a practical moderator if it has a large neutron absorption cross section.

Table 3.4: Moderation power and moderation ratio of commonly used moderators.

Moderator	Moderation Power	Moderation Ratio
H_2O	1.28	2.5
D_2O	0.18	2.1×10^4
Be	0.16	130
Graphite	0.064	200
Polyethylene	3.26	122

Table 3.4 shows the moderation power and moderation ratio of several commonly used moderators. Although heavy water seems to be a better moderator with a much higher moderation ratio because of its low absorption cross section, regular water is favorable due to lower cost and wide availability. Other solid materials can also be used for moderation and shielding purposes. In this study water and polyethylene were mainly used for neutron moderation and shielding.

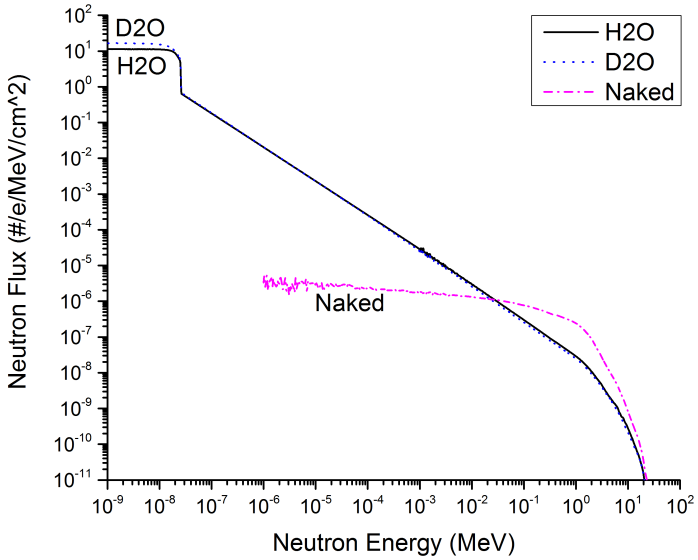

Figure 3.8: MCNPX neutron flux distribution as a result of using different type of moderator in a one cubic feet tank.

A set of MCNPX simulations was carried out to find an optimum neutron moderator for 40 MeV electron induced photoneutrons. Water and heavy water were the best moderators with a given volume. Polyethylene is a great moderator but requires a bigger volume of material to moderate the same amount of neutrons (Fig. 3.8).

A neutron reflector is often used to guide neutrons in a certain direction or simply to minimize the neutron loss in a volume (Fig. 3.9). Low and high Z materials can be used as reflectors based on the neutron energy. Low Z materials are often used for thermal

neutron reflection and higher Z materials are used for fast neutrons. For example, Be is a particularly good reflector because of low energy secondary neutron production, while Ni has been used extensively as a fast neutron reflector.

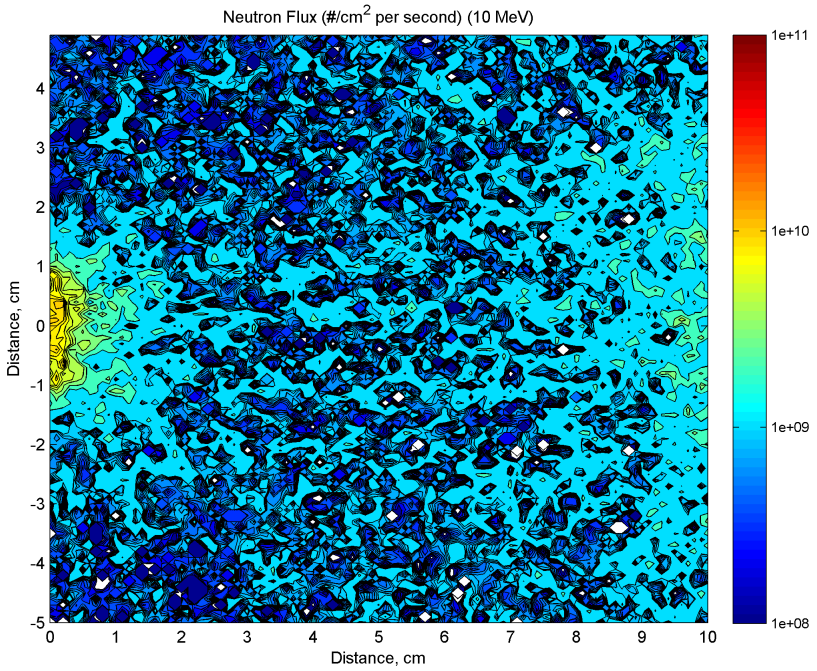

Figure 3.9: An example of neutron flux distribution showing clear neutron reflection. MCNPX simulations include a 10 MeV electron incident on a 0.25 cm LBE converter followed by a 10 cm by 10 cm D_2 gas chamber as a neutron source. The D_2 gas is surrounded by Pb which serves as a neutron reflector.

3.4 Mixed-Field of Neutrons and Photons

In the past, transmutation studies have generally been focused on single particle irradiation schemes. Here we would like to explore the feasibility of using two particle irradiation: photon and neutron. In this scheme both photons and neutrons transmute a

single isotope to two different isotopes or transmute two different isotopes to one single isotope. By using mixed-field irradiation, transmutation efficiency can be improved.

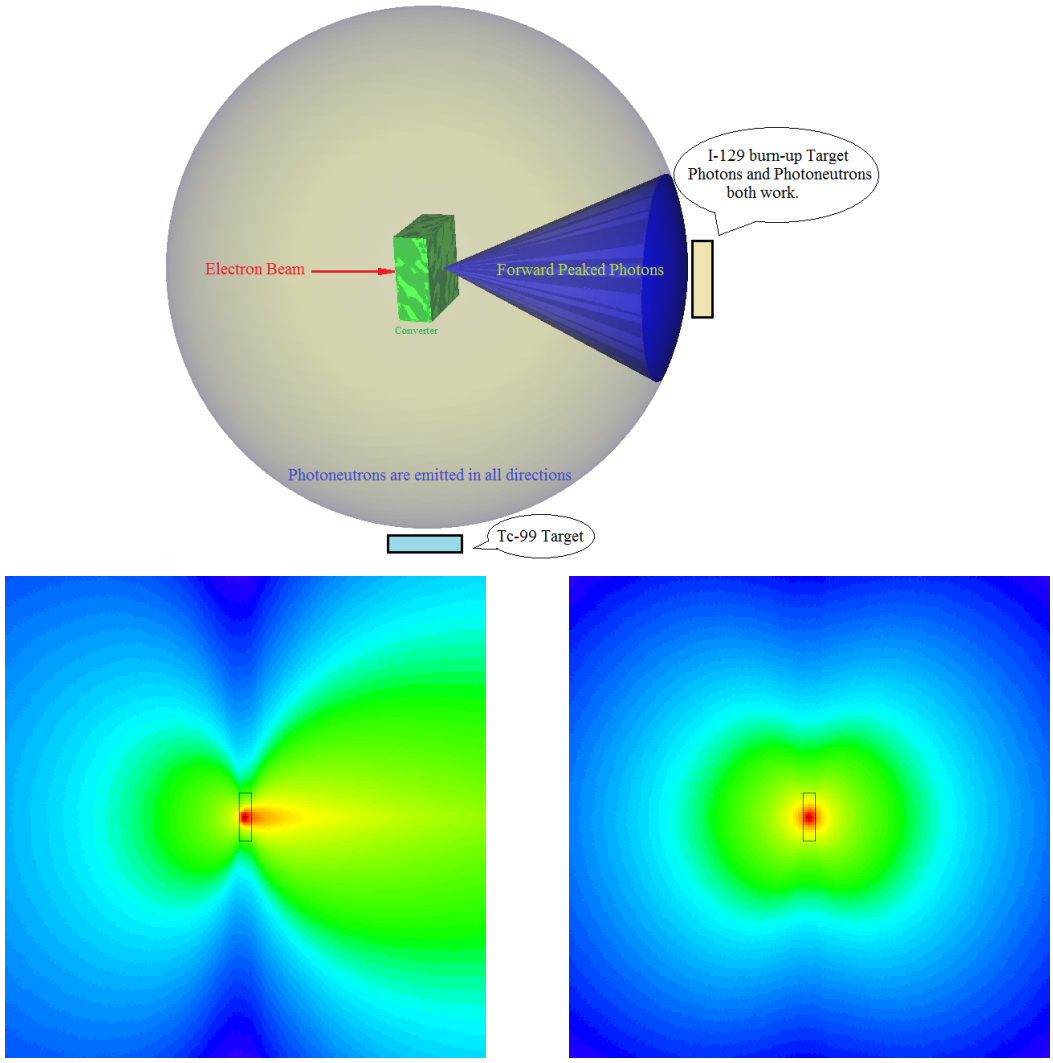

Figure 3.10: Transmutation scheme of ^{129}I and ^{99}Tc using mixed or single radiation field (top); MCNPX generated photon (bottom left) and neutron (bottom right) distributions. MCNPX simulations include a 40 MeV electron beam incident on 1 cm thick, 2 cm by 2 cm tungsten plate. Irregularities come from the geometry of the converter and the beam size (1 cm in diameter).

The major issue in developing an efficient mixed-field transmutation scheme is proper target design to optimize both photon and neutron production. This must be done in such a way that the thermal and mechanical properties of the system are practical and cost effective. An illustration of the mixed irradiation idea is shown in Fig. 3.10 as an example of resolving the ^{129}I and ^{99}Tc problem in LLFP.

It is obvious that optimization of mixed-field production is very case-dependent. Parameters of the incident electron beam, properties of the target material, operation conditions and types of nuclear interactions are the determining factors of the optimization. Therefore, the mixed-field concept will be carried out in the following sections along with specific cases.

3.5 Transmutation of LLFPs and Surrogates

A feasibility study of LLFP transmutation is of particular interest to assess the practicality of linac based nuclear waste management. The classes of nuclear reactions to be exploited include (n,γ) and (γ,n) reactions, since both of them have the capability of transmuting certain isotopes towards stable or short-lived nuclides. For example, the particular nuclear properties of ^{99}Tc and ^{129}I are such that a burn-up transmutation reaction for ^{99}Tc requires only neutrons (^{99}Tc(n,γ)^{100}Tc), while a burn-up transmutation reaction for ^{129}I can use both neutrons and photons producing shorter half-life products (^{129}I(n,γ)^{130}I and ^{129}I(γ,n)^{128}I). As a proof of principle, simple converter and target design schemes that can be easily tested experimentally were introduced.

3.5.1 ^{99}Tc Single-Field Transmutation

In ^{99}Tc burn-up, only the ^{99}Tc(n,γ)^{100}Tc reaction is useful in producing ^{100}Tc with a half-life of 15.8 seconds. The ^{99}Tc(γ,n)^{98}Tc should be strongly suppressed since it produces ^{98}Tc which has a half-life of 4.2 million years. This calls for a pure neutron radiation field free of any excessive GDR-photons.

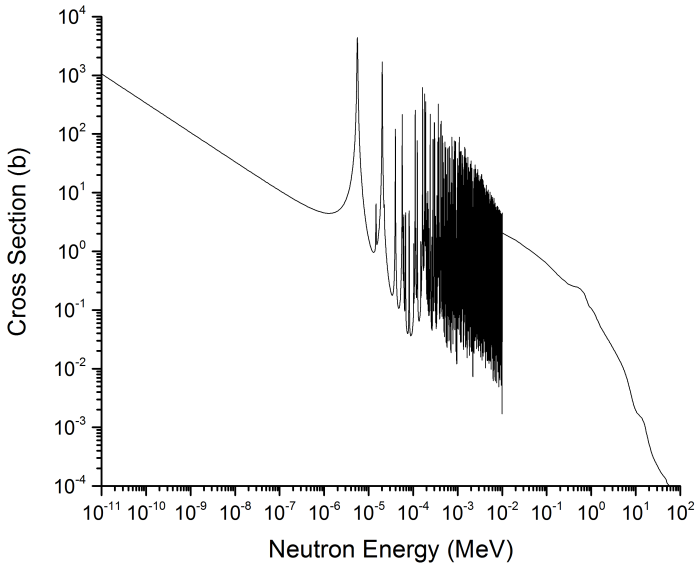

Figure 3.11: ^{99}Tc(n,γ)^{100}Tc reaction cross section [48].

The ^{99}Tc neutron capture cross section suggests the use of a moderator for effective transmutation (Fig. 3.11). Two scenarios were examined to minimize the effect of the photon radiation field (Fig. 3.12). The first one is to distribute the ^{99}Tc target so that it surrounds a 2 cm thick W converter around the sides and the back. The second setup is to attenuate the photons before they reach the ^{99}Tc target by using water moderator between the W converter and target material.

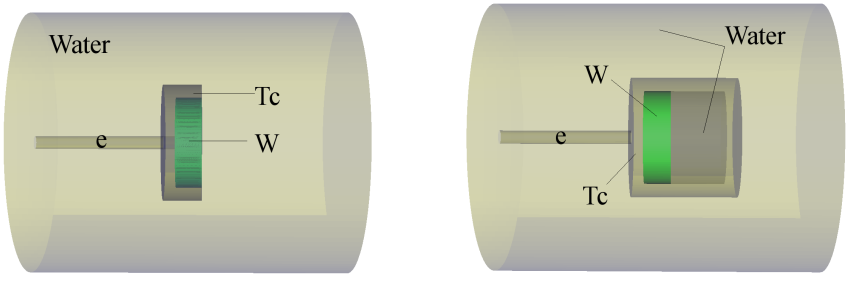

Figure 3.12: Two setup scenarios for ^{99}Tc transmutation.

MCNPX simulations were done for the above two scenarios using a 2 cm thick tungsten converter and a 40 MeV electron beam. Reaction yields were calculated and tabulated in Table 3.5 to compare different cases. The goal was to minimize ^{98}Tc production and maximize ^{100}Tc production by varying the moderator volume.

Table 3.5: Optimization of ^{99}Tc neutron-field transmutation by different target design. By varying the photon travel distance in the water, ^{100}Tc and ^{98}Tc production rates were calculated. The results are subject to a maximum of 10% uncertainty.

Setup	H_2O Thickness (cm)	H_2O Volume (cm^3)	Transmutation Rate (#/cm^3/e)	
			^{99}Tc(n,γ)^{100}Tc	^{99}Tc(γ,n)^{98}Tc
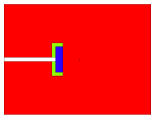	0	0	**5.1E-6**	**2.1E-8**
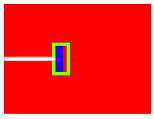	1	38.5	9.2E-6	2.1E-6
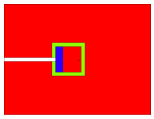	5	192.5	5.4E-6	6.4E-7
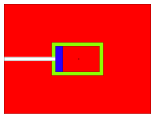	10	385	1.8E-6	2.2E-7
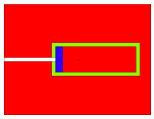	20	770	1.2E-7	4.9E-8

It turned out that the first setup where the target material is distributed around the sides and back of the tungsten converter yields the best result regarding a lower photoproduction rate of ^{98}Tc. In the second setup, significant reduction of ^{98}Tc photoproduction needs a larger moderator volume and it comes at the cost of a low production rate of ^{100}Tc. Therefore, as a simple setup, the first design (Fig. 3.12) should be used in order to

minimize the effect of the photon field and to maximize the use of the neutrons.

3.5.2 ^{129}I Mixed-Field Transmutation

The (γ,n) reaction of ^{129}I has a threshold energy of 8.84 MeV. Therefore only photons above this energy are useful for iodine burn-up. In the case of neutrons, although the photoneutron flux is approximately two orders of magnitude lower than the photon flux, thermalized neutrons can enhance the reaction rate such that the burn-up efficiency of iodine can be significantly increased (Fig 3.13). Therefore, both ^{129}I(γ,n)^{128}I and ^{129}I(n,γ)^{130}I are useful in producing ^{128}I and ^{130}I burn-up products with half-lives of 25 minutes and 12.36 hours, respectively.

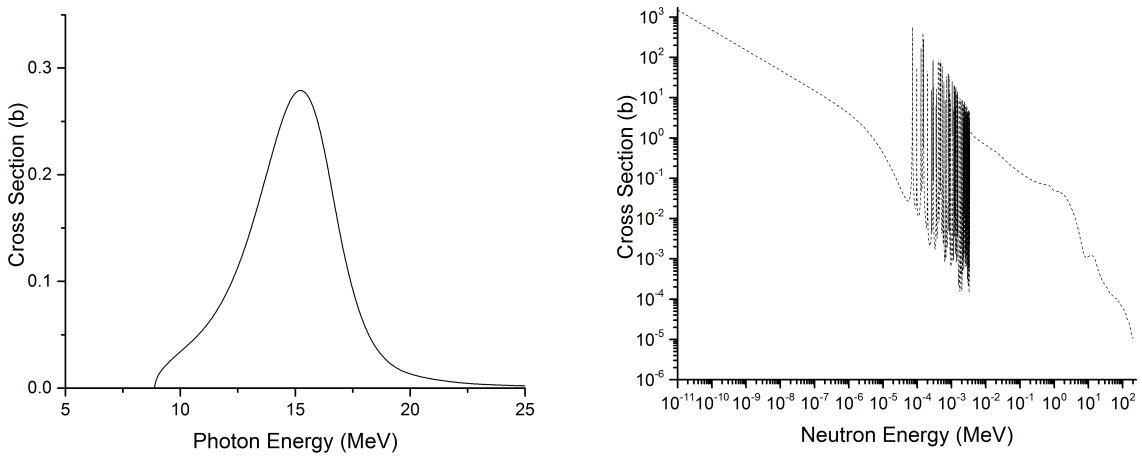

Figure 3.13: ^{129}I(γ,n)^{128}I (left) and ^{129}I(n,γ)^{130}I cross section (right), adapted from [48].

Two scenarios were considered (Fig 3.14) for the ^{129}I transmutation. First, a common converter was used for photon and neutron production. In this setup, the target material is distributed around the converter and is surrounded by a neutron moderator. Alternatively, two separate converters were used for photon and neutron production. In this case, the neutron converter was surrounded by the target material and moderator.

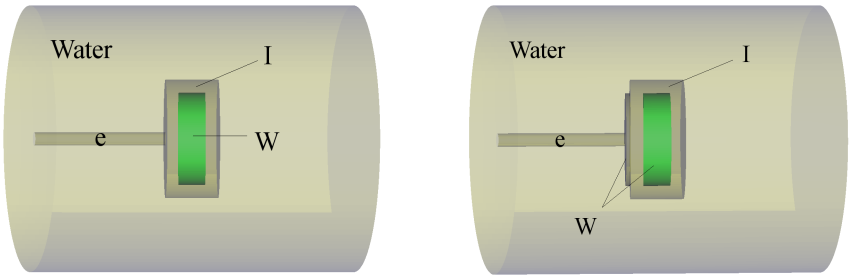

Figure 3.14: Design setup for ^{129}I transmutation.

In the first design, to generate adequate neutron flux, a thicker converter has to be used which limits the maximum photon production. However, in the second design both photon and neutron fields can be utilized effectively because it takes full advantage of an optimum photon field plus a neutron field produced by the photons in the second converter.

Table 3.6: Optimization of ^{129}I mixed-field transmutation; a single tungsten converter was used. By varying the converter thickness, ^{130}I and ^{128}I production rates were calculated. The results are subject to a maximum of 10% uncertainty.

Converter Thickness (cm)	Transmutation Rate (#/cm^3/e)		
	^{129}I(n,γ)^{130}I	^{129}I(γ,n)^{128}I	Sum
0.35	5.8E-6	**2.9E-5**	**3.48E-5**
0.6	7.1E-6	2.2E-5	2.91E-5
1	8.6E-6	1.3E-5	2.16E-5
2	9.5E-6	3.7E-6	1.32E-5
5	7.8E-6	6.2E-7	8.42E-6

MCNPX simulations were performed to obtain the maximum reaction rates of both ^{129}I(γ,n)^{128}I and ^{129}I(n,γ)^{130}I. In the first design setup (Table 3.6), the thickness of the tungsten converter was the variable. The results show the dominance of ^{129}I(γ,n)^{128}I reaction through photon field. This setup yields a best result of 3.48E-5 (reaction per cm^3) when the thickness is around 0.35 cm, which is the optimum photon production

thickness. Although the neutron induced transmutation rate peaks when the converter thickness is around 2 cm, the dominance of the photo-induced transmutation suggests a thinner material as the common converter.

In the second design setup (Table 3.7), the first converter thickness was set at 0.35 cm and the second converter thickness was the variable. By varying the second converter thickness, we can see that the ^{129}I(n,γ)^{130}I reaction contributes to the total transmutation rate while the ^{129}I(γ,n)^{128}I reaction rate do not change significantly. Varying the thickness of the second converter, we found the maximum total transmutation rate to be 7.5×10^{-5} (reaction per cm^3), which is almost twice as high as transmutation rate for the single converter setup.

Table 3.7: Optimization of ^{129}I mixed-field transmutation using two W converters were used. By varying the second converter thickness, ^{130}I and ^{128}I production rates were calculated. The results are subject to a maximum of 10% uncertainty.

Converter Thickness (cm)	Transmutation Rate (#/cm^3/e)		
	^{129}I(n,γ)^{130}I	^{129}I(γ,n)^{128}I	Sum
0.2	1.1E-5	3.2E-5	4.3E-5
0.5	1.3E-5	**6.2E-5**	**7.5E-5**
1	1.4E-5	4.6E-5	6.0E-5
1.5	1.4E-5	3.7E-5	5.1E-5
2	1.3E-5	3.2E-5	4.5E-5

Furthermore, two separate converter designs should be used in order to increase the transmutation rate of ^{129}I by the dual-irradiation scheme. Note that the second converter serves as an enhancement by generating neutrons from the residue photons from the first converter. The generated neutrons will be moderated and absorbed by the ^{129}I nucleus so that the total burn-up rate is increased.

3.5.3 ^{99}Tc and ^{129}I Surrogate

With current techniques, ^{99}Tc and ^{129}I are hard to separate from the nuclear waste in a favorable compound form [14]. Even if they are separated, they are hard to handle due to high radiotoxicities. Therefore surrogate materials are necessary to experimentally confirm our simulations of the transmutation efficiency. Surrogate materials were found for ^{99}Tc and ^{129}I based on nuclear properties. A surrogate should have similar fundamental nuclear/atomic properties and similar nuclear reaction cross section. A surrogate material has to undergo a similar nuclear reaction and should produce a detectable product with a favorable radiation signature (half-life and γ-energy). A surrogate material should be easy to handle and obtain, and should have similar reaction rates under the same irradiation conditions.

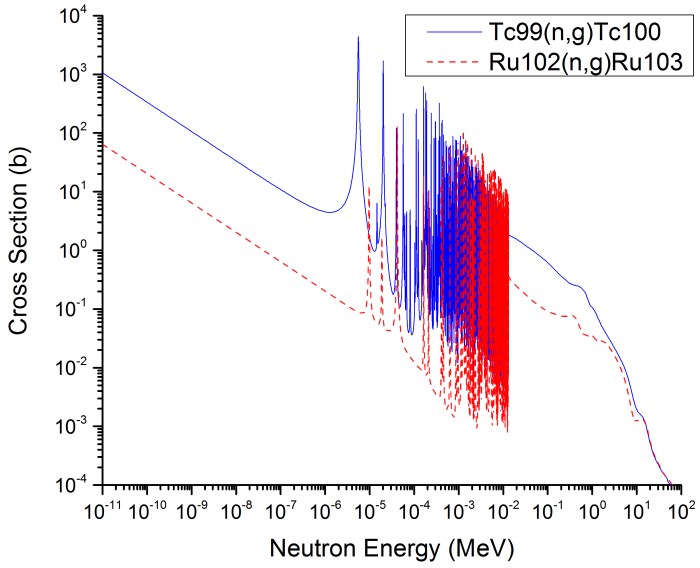

Figure 3.15: ^{99}Tc(n,γ)^{100}Tc and ^{102}Ru(n,γ)^{103}Ru reaction cross sections.

In case of ^{99}Tc, several isotopes were considered such as ^{98}Mo,^{102}Ru, and ^{102}Pd. ^{102}Ru turned out to be the best option due to a similar neutron absorption cross section, ease of handling, and a detectable product isotope. However, a scaling factor of 19 needs

to be used for the reaction rate comparison because of the difference between the total integrated cross sections (Fig. 3.15). MCNPX simulations were performed using the first design setup as shown in Fig. 3.12. ^{99}Tc(n,γ)^{100}Tc and ^{102}Ru(n,γ)^{103}Ru reaction rates were found to be 7.1×10^{-6} and 3.9×10^{-7} reactions per cm^2 respectively. After scaling the reaction rate by the scaling factor of 19, their reaction rate values were similar. So ^{102}Ru was a good candidate as the surrogate of ^{99}Tc for the purpose of transmutation studies.

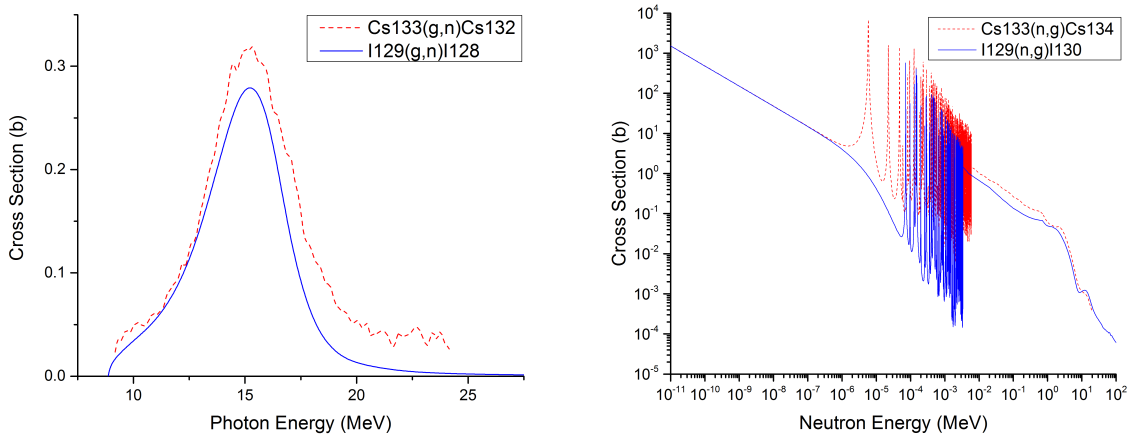

Figure 3.16: (γ, n) and (n, γ) reaction cross sections for ^{129}I and ^{133}Cs, adapted from [48].

In case of ^{129}I, surrogate material requirements were even tighter since it had to satisfy the conditions of mixed-field transmutation scheme. ^{133}Cs was the only suitable candidate when both nuclear properties and (γ,n)/(n,γ) reaction cross sections were taken into considerations (Fig. 3.16). MCNPX simulation results of ^{133}Cs and ^{129}I reaction rate calculations show that Cs can be used as an surrogate for ^{129}I with similar reaction rates. Experimental studies of Ru and Cs as surrogates are discussed in Chapter 4.

3.6 Radioisotope Production

Many radioisotopes can be produced by electron accelerators. A few of them can

be optimized using the mixed field technique. ^{47}Sc and ^{64}Cu are the examples of useful radioisotopes which can be produced using the mixed-field irradiation scheme. Based on their nuclear properties, ^{47}Sc can be produced by ^{47}Ti(n,p)^{47}Sc and ^{48}Ti(γ,p)^{47}Sc reactions from two stable isotopes of titanium, while ^{64}Cu can be produced by ^{63}Cu(n,γ)^{64}Cu and ^{65}Cu(γ,n)^{64}Cu reactions from two stable isotopes of copper. Table 3.8 shows nuclear properties of ^{47}Sc and ^{64}Cu.

Table 3.8: Properties of ^{47}Sc and ^{64}Cu.

Radioisotope	Half-Life	Decay Mode	Gamma Energy
^{47}Sc	3.35 d	β^- : 100%	159.38 keV
^{64}Cu	12.7 h	β^+ : 61.5%; β^- : 38.5%	1346 keV

In case of ^{47}Sc production, although the neutron radiation field is less intense than the photon field, a higher and flatter (n,p) reaction cross section suggests that neutron irradiation might have a significant contribution to the overall production rate. Neutron moderation is not necessary in ^{47}Sc production since neutron absorption cross section peaks in the MeV region (Fig. 3.17). Table 3.9 shows the target nuclide abundance, primary reactions of interest, reaction threshold, and product isotope's half-lives and gamma energies. All the reaction cross sections are shown in Fig. 3.17.

Table 3.9: Photon and neutron induced reactions of titanium.

Reaction	Threshold	Target Abundance	Product Half-Life	γ-Energy
^{46}Ti(γ,np)^{44}Sc	21.7 MeV	8.25%	3.92 hours	1159 keV
^{47}Ti(γ,p)^{46}Sc	10.5 MeV	7.44%	2013 hours	889, 1120 keV
^{47}Ti(n,p)^{47}Sc	0.69 MeV	7.44%	82.32 hours	159 keV
^{48}Ti(γ,p)^{47}Sc	11.4 MeV	**73.72**%	82.32 hours	159 keV
^{49}Ti(γ,p)^{48}Sc	11.4 MeV	5.41%	43.92 hours	983, 1040, 1314 keV

MCNPX simulations were carried out to calculate production rates of the desired isotope as well as all the possible byproducts created by photon/neutron induced reactions

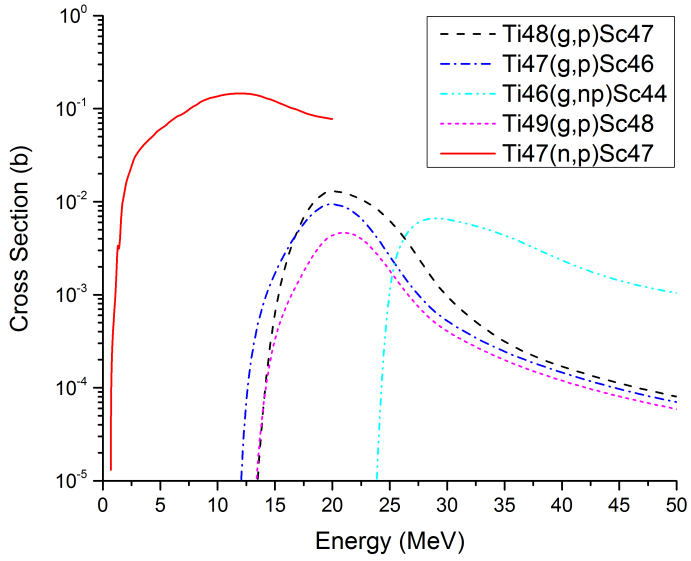

Figure 3.17: Photon and neutron induced reaction cross sections for Ti isotopes.

(Table 3.10). The results show that the contribution of ^{47}Ti(n,p)^{47}Sc was insignificant compared to the photo-production of ^{47}Sc via ^{48}Ti(γ,p)^{47}Sc reaction. This can be explained by low fast neutron flux that is useful for neutron-induced production. The results also show that a considerable amount of ^{44}Sc and ^{48}Sc will be created but can be suppressed by choosing a lower electron beam energy (< 21.7 MeV).

Table 3.10: Reaction type and production yield of Sc isotopes. MCNPX simulation results are shown using a 40 MeV electron incident on a 0.35 cm thick tungsten converter. The results are subject to a maximum of 10% uncertainty.

Reaction	Production Rate (μCi/C/g)
^{46}Ti(γ,np)^{44}Sc	4.6
^{47}Ti(γ,p)^{46}Sc	1.9
^{47}Ti(n,p)^{47}Sc	13
^{48}Ti(γ,p)^{47}Sc	**245.1**
^{49}Ti(γ,p)^{48}Sc	28.9

In case of ^{64}Cu, its nuclear properties and natural abundance makes it an excellent candidate for a mixed field transmutation. Natural copper consists of ^{63}Cu (69.15%) and ^{65}Cu (30.85%). Thus, ^{64}Cu can be produced through both ^{63}Cu(n,γ)^{64}Cu and ^{65}Cu(γ,n)^{64}Cu channels. Fig. 3.18 shows the cross sections of both reactions.

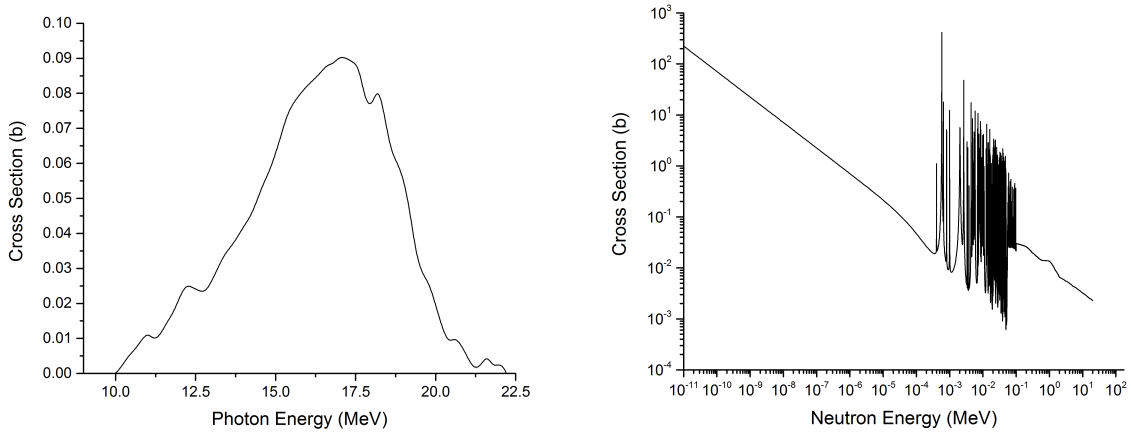

Figure 3.18: (γ,n) and (n,γ) reaction cross sections for ^{65}Cu and ^{63}Cu, adapted from [48].

MCNPX simulations were done using the double-converter type design shown in Fig. 3.14. Production rates of ^{64}Cu were calculated and tabulated in Table 3.11. The results show that using the mixed-field irradiation can improve ^{64}Cu production rate by 30%, compared to the single field production. Note that the simulations were done using a simple setup where the moderator and reflector setups were not optimized. Even better production rates can be expected using a complex model taking full advantage of the mixed-field irradiation scheme.

Therefore, the photon field irradiation scheme is useful for ^{47}Sc production yielding 245 μCi per Coulomb of charge per gram of Ti metal. ^{64}Cu production can be improved by using the mixed-field irradiation scheme with a production rate of 21 μCi per Coulomb of charge per gram of Cu metal. It is obvious that by using an enriched ^{48}Ti target, an even higher yield of ^{47}Sc can be achieved. Also, in this case, the ^{47}Sc will be free of byproduct

Table 3.11: Reaction type and production yield of Cu isotopes. MCNPX simulation results are shown using a 40 MeV electron incident on a 0.35 cm thick tungsten converter. The results are subject to a maximum of 10% uncertainty.

Reaction	Production Rate (μCi/C/g)
^{65}Cu(γ,n)^{64}Cu	16
^{63}Cu(n,γ)^{64}Cu	5

isotopes such as ^{44}Sc and ^{48}Sc. However, production of such byproducts can be minimized by adjusting the electron beam energy. An experiment is discussed in Chapter 4 using a 22 MeV electron beam to benchmark the simulation results of ^{47}Sc production.

Chapter 4

Experimental Setup and Results

Experimentations are the important means of benchmarking to ensure the reliability of computer modeling. Feasibility and technical aspects can be developed and improved by useful apparatus design and measuring methods. In this Chapter, the apparatus setup and design is described, activation and radioactivity measurement techniques are introduced, and LLFP surrogates, as well as potential radioisotope experimental studies are discussed to address the feasibility of the mixed-field irradiation technique.

4.1 Apparatus

The Idaho Accelerator Center (IAC) is a unique research facility operated by Idaho State University located in southeast Idaho [44]. The IAC has three laboratories: on the main campus, in the Business and Research Park, and at the Pocatello Airport. They serve as a principal investigating conduit for R&D in nuclear physics applications in material science, biology, homeland and national security. All the work described in this dissertation was performed at the Business and Research Park, a laboratory which houses several electron linacs, and a nuclear counting lab for spectroscopy analysis.

4.1.1 Electron Accelerators

Two linacs were mainly used for this study:

- 44-MeV Short-Pulse Electron Linac. This machine is an RF linear accelerator operating at the L-band frequency of 1428 MHz. Three experimental ports are available:

the 90 degree port offers a beam energy-analyzed to 1 to 10%, depending on the slit position; the 0 degree port produces slightly higher beam currents, but is not well defined in energy. A trigger synchronous with the electron beam (<10 ps) is available for timing and repetitive sampling experiments. Electron energies range from 2 to 44 MeV, and pulse width is 50 ps to 2 μs. The maximum power is about 2 kW.

- 48-MeV 10-kW High Power Linac: This machine is an RF linear accelerator operating at the S-band frequency of 2856 MHz. Two experimental ports are available: the 45 degree port which is mainly used for beam monitoring and tuning; the 0 degree port is mainly used for high power irradiation. Electron energy ranges from 28 to 48 MeV. The pulse width varies from 100 ns to 8 μs and average current ranges from 10 to 500 μA. The maximum power is 10 kW at 40 MeV energy.

The above two machines are often referred as the L-band linac and Jack respectively. Prior to each experiment, engineers tune the linacs so that the requested beam parameters (i. e. beam size, average beam current, and peak beam energy) are achieved.

4.1.2 Gamma Spectrometry

In the IAC's nuclear counting lab, there are two HPGe detectors that were used extensively for this work. The data acquisition system consists of a HPGe detector, ORTEC 672-type amplifier, analog-to-digital converter, and MPA-3 multiparameter system which is a fast list-mode multichannel data acquisition system.

The two HPGe detectors, named as Det-A and Det-D, have energy resolutions of 2 keV and 1.8 keV at 1.3 MeV. Their detectable photon energy ranges from 40 keV to above 3 MeV. An excellent peak to Compton-background ratio makes them even more suitable for the detection of higher energy photons (> 400 keV). In order to achieve an acceptable dead time, several positions are available to place samples for each detector. Sample positions were chosen depending on sample geometry and radioactivity. Efficiency

curves exist for all predetermined positions. Available positions and detector efficiencies are shown in Fig. 4.1.

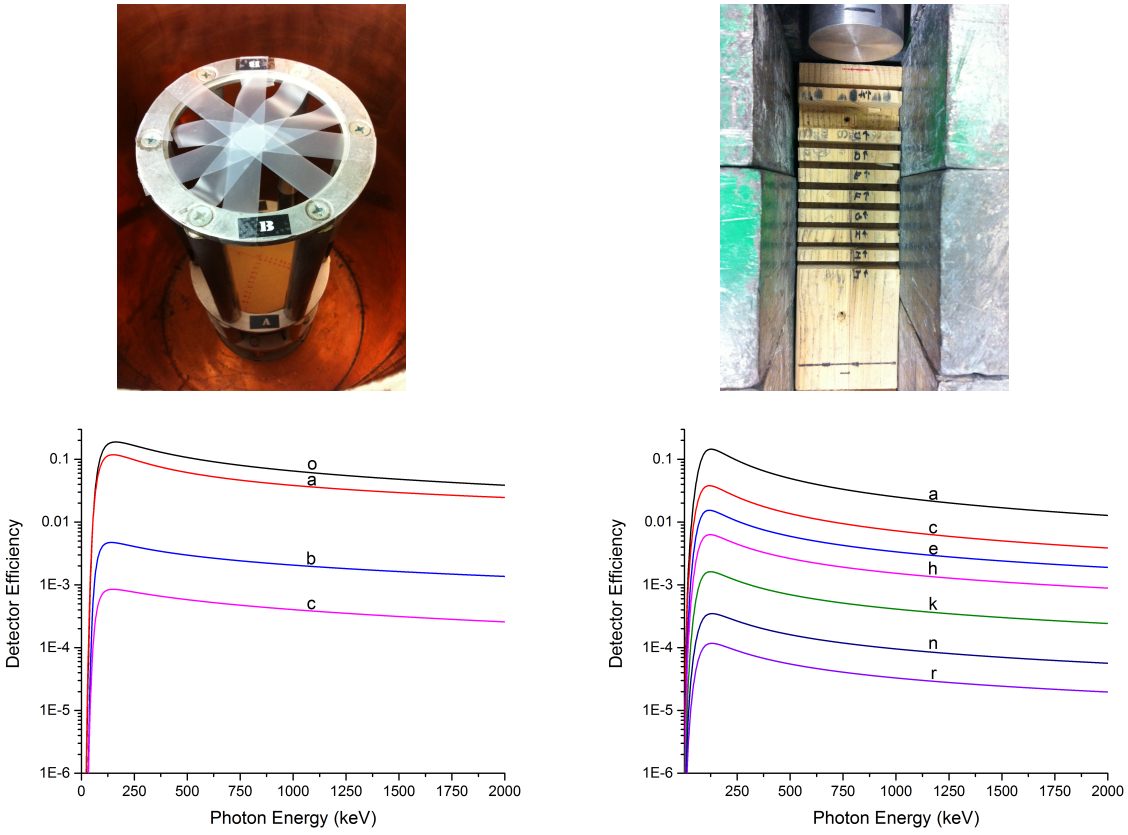

Figure 4.1: HPGe detector counting positions and its efficiency curves. [45]

Before each gamma spectroscopy measurement (counting), an energy calibration of the detector was performed. Numerous radioactive calibration sources, such as ^{60}Co, ^{133}Ba, and ^{133}Cs, were used to cover gamma energies ranging from tens of keV to several MeV.

A typical spectrum obtained by MPA3 is shown in Fig. 4.2. When a particular gamma energy region is selected, a Gaussian fitting function can be used to provide total counts under the peak. Thus, based on the peak gamma energy and the total counts registered within the peak, radioactivity of the samples can be calculated using the formulations described in Chapter 2.

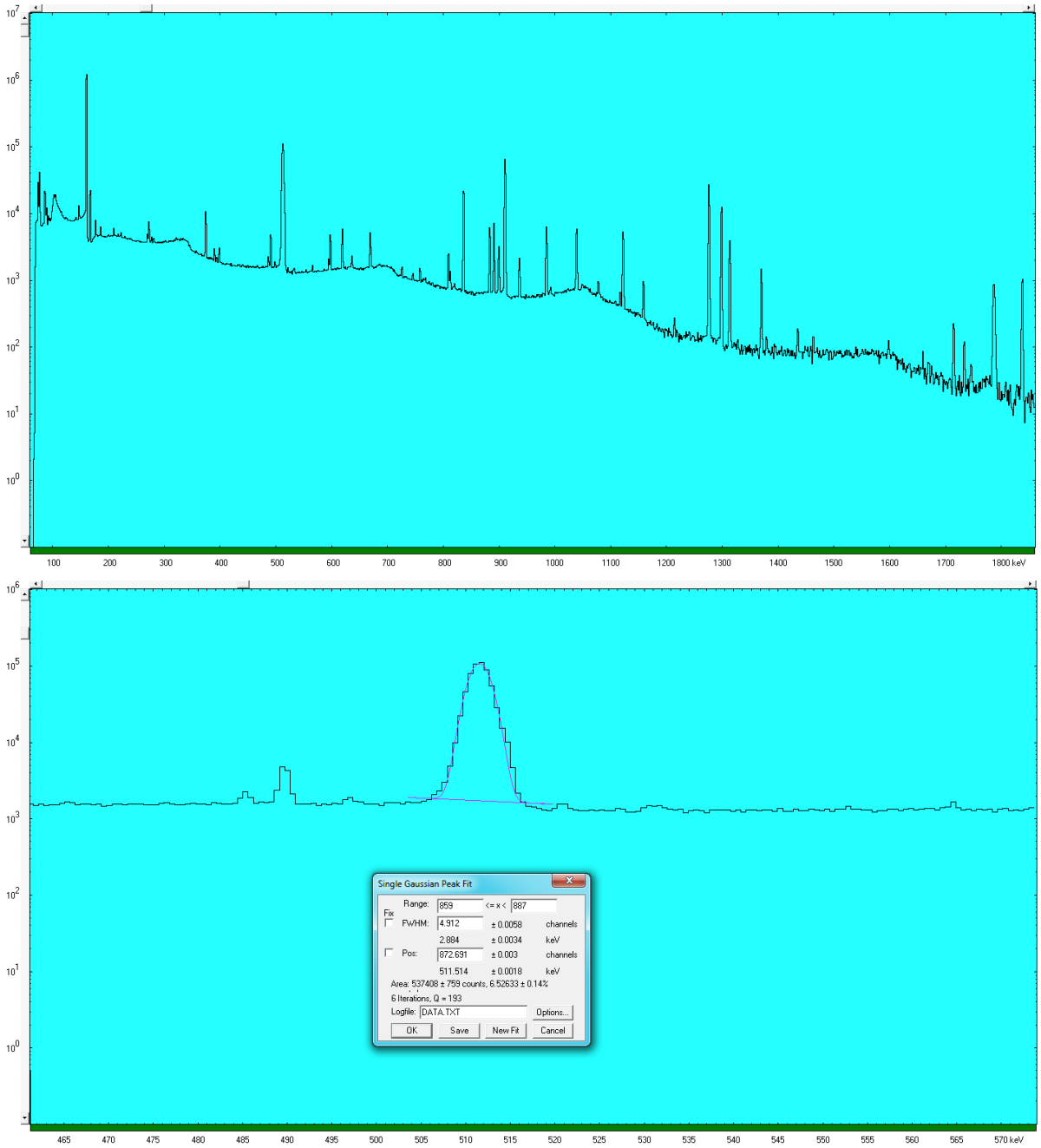

Figure 4.2: MPA software screen-shots illustrating a typical gamma spectrum and a built-in Gaussian fitting function.

4.1.3 Neutron Time-of-Flight Setup

The TOF system consists of 5 plastic scintillators each having a cylindrical shape, 5.08 cm in length and diameter, coupled with time measurement electronics. The plastic scintillator used was a BC-408 type material utilizing a polyvinyltoluene (C_9H_{10}) base doped with special organic molecules that emit visual light when the electron structure of these molecules is excited. Its fast rise and short decay times, 0.9 and 2.1 ns, allows data acquisition with great time resolution. Fast photomultiplier tubes were mounted on the plastic scintillators and covered with layers of black non-transparent tape. Raw detector signals from each plastic scintillator were constant fraction discriminated using an ORTEC model CF8000, and then sent to certain channels of a time-to-digital (TDC) converter CAEN V1290/n. A detailed description of the TOF system can be found in [49].

4.2 Experiments and Results

4.2.1 Activation Method for Flux Measurements

If a metal wire/foil is placed in a photon or neutron field, the nuclear reaction product's activity can be used as an indicator of the photon or neutron flux. For intense photon field measurement, there are many options available since many photonuclear reactions have well-known measured cross-sections, particularly photoneutron reactions. For neutron field measurements, any influence from gamma radiation should be suppressed. For example, a photonuclear reaction such as (γ,n) will interfere with (n,2n) for fast neutron flux measurement, which leaves us with fewer options. Table 4.1 shows several possible reactions for activation-based field measurement method. Aluminum can be used as the fast neutron flux monitor since Al^{27}(n,α)Na^{24} reaction has a threshold energy of 3.25 MeV, while gold and manganese can be used for whole neutron spectrum measurements.

Table 4.1: Possible reactions for flux measurement.

	Reaction	T	E (keV)	E_{th} (MeV)
Al	^{27}Al(n,α)^{24}Na	15.03 h	1369, 2754	3.25
Cu	^{65}Cu(γ,n)^{64}Cu	12.7 h	1346	9.91
Mn	^{55}Mn(n,γ)^{56}Mn	2.58 h	847, 1811, 2113	0
Au	^{197}Au(γ,n)^{196}Au	6.2 d	333, 356, 426	8.07
Au	^{197}Au(n,γ)^{198}Au	2.695 d	412, 676, 1088	0
Au	^{197}Au(n,2n)^{196}Au	6.2 d	333, 356, 426	8.112

4.2.2 Flux Measurements and Benchmarking

In order to understand the neutron and photon radiation field produced by a high energy electron beam, a tungsten-copper (80%-W, 20%-Cu compound is easily machinable) converter was used as a target. Fig. 4.3 shows the target geometry and flux monitors. Alloy wires (84% Cu, 12% Mn, and 4% Ni) were used for photon and neutron flux monitoring. The wires were inserted into the pre-drilled holes of the 6 cm by 6 cm cylindrical shaped tungsten converter to map out the radiation field distributions inside the thick converter. The samples were irradiated for 30 minutes using a 40 MeV electron beam at 110 W beam power.

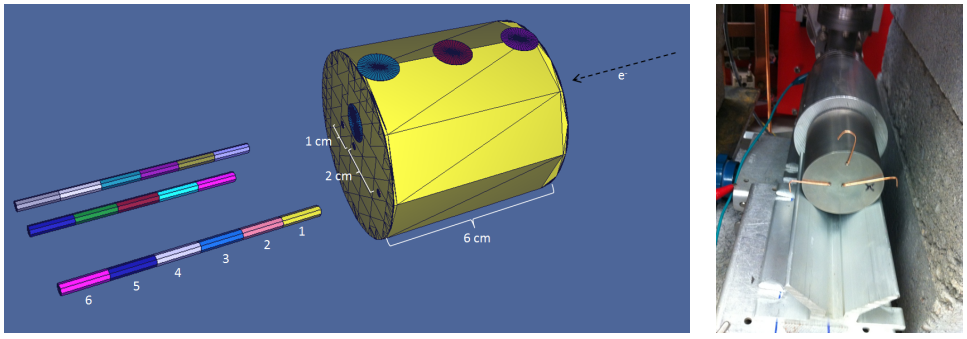

Figure 4.3: Target geometry and positions of the holes: center, 1 cm off axis, and 2 cm off axis (left). Actual setup and the positions of the wires (right).

After the irradiation, the wires were cut into pieces (1 cm each) for the activity analysis. ^{65}Cu(γ,n)^{64}Cu reaction was used for the photon flux measurement, while the ^{55}Mn(n,γ)^{56}Mn reaction was used for the neutron flux measurement. Meanwhile, MCNPX simulations were performed to predict the photon and neutron fluxes and the resulting activities of ^{64}Cu and ^{56}Mn. Activities of the samples are shown in Fig. 4.4 where the lines are the predicted activities for each wire and the dots are the measured activities for each piece of the sample. The discrepancy between the simulation and the measurement is around 30%. Both MCNPX simulation and experimental results show that as one goes away from the vertex, both neutron and photon flux decrease significantly.

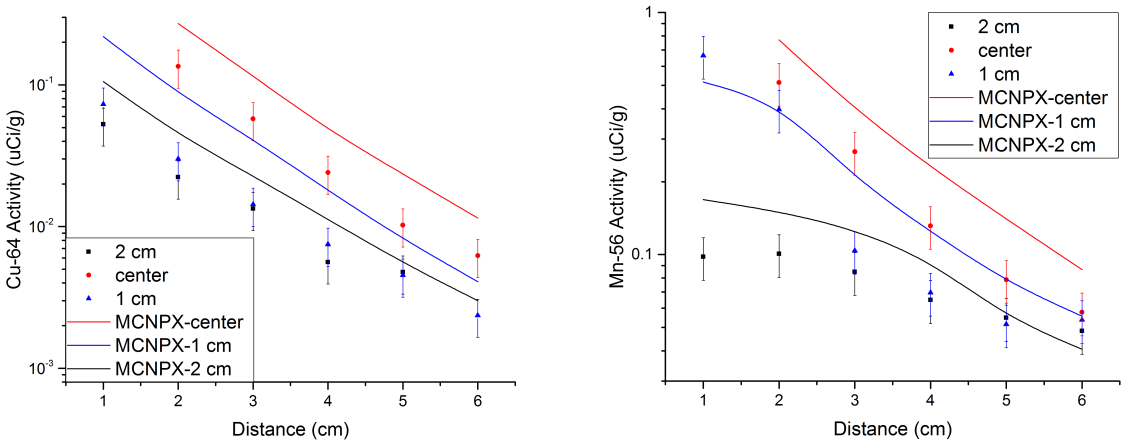

Figure 4.4: Photon and neutron flux gradient along the converter measured by activation method. Activities of ^{64}Cu along the line of center, 1 cm, and 2 cm off axis wires (left). Activities of ^{56}Mn along the lines of 3 wires (right).

A second experiment was conducted using Al wires to map out the fast neutron flux distribution around the thick tungsten converter. ^{27}Al(n,α)^{24}Na reaction was used for the fast neutron flux measurement. The 6 cm by 6 cm tungsten-copper converter was used for the efficient production of photoneutrons. Al wires were placed at different locations around the converter as a "saddle" (Fig 4.5). The samples were irradiated for 30 minutes

using a 40 MeV electron beam at 110 W beam power.

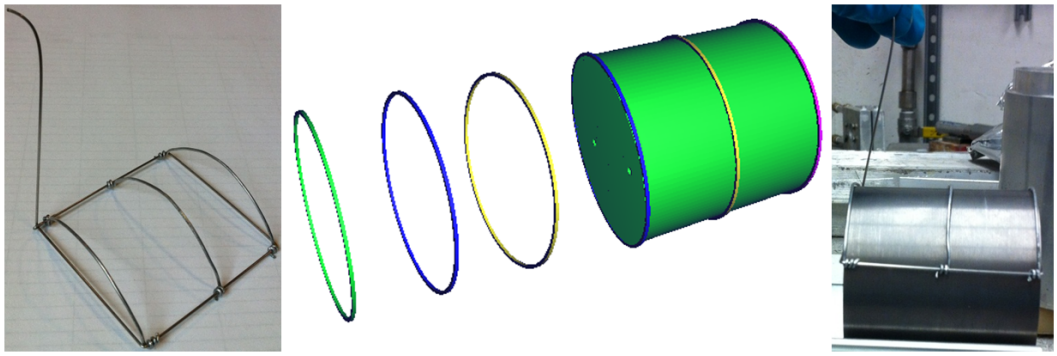

Figure 4.5: Saddle-shaped activation wires around the converter.

By comparing MCNPX and experimental results, we see that there is a significant disagreement between fast neutron production predictions and experimental data (Fig. 4.6), where experimental results are higher than the simulation. The model cross section data for ^{27}Al(n,α)^{24}Na reaction [48] and sodium contamination from sample handling during preparation might well be the reason for this discrepancy (Appendix B).

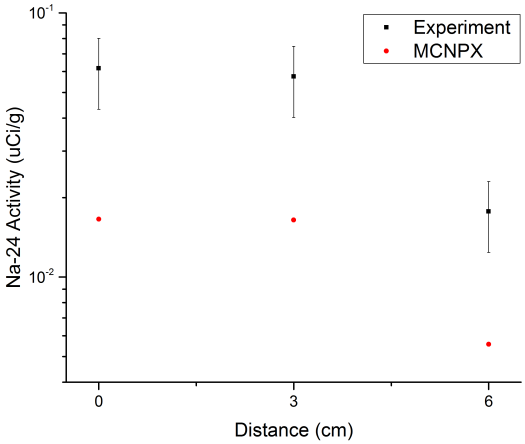

Figure 4.6: Comparison of MCNPX and experimental results of activities of ^{24}Na using saddle-shaped wires around the converter.

To verify neutron moderation calculations by the simulation method, two sets of irradiations were done using the same cylindrical shaped tungsten-copper converter in a cubic-foot tank. Four gold foils were placed on the top, left, right, and the back of the tungsten converter. The reaction of interest was ^{197}Au(n,γ)^{198}Au for neutron flux estimation. The tank was empty in the first experiment and filled with water in the second set of irradiation. Each experiment had a 2 hour-long irradiation with a 40 MeV electron beam at 10 W of power (low power was chosen to avoid a possible water boiling). Experimental set up is shown in Fig. 4.7

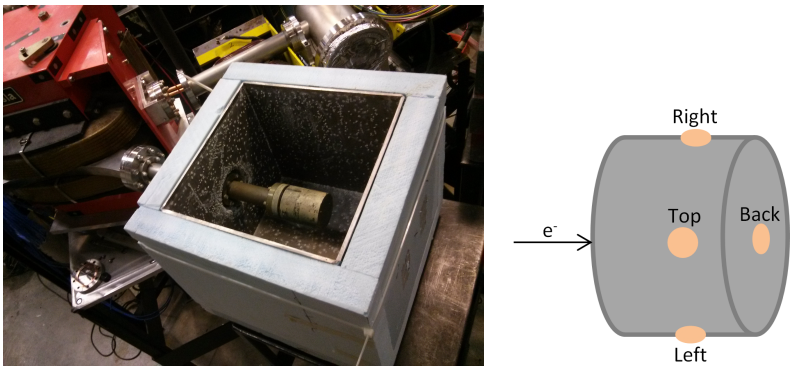

Figure 4.7: Experimental setup of gold foil activation. Four gold foils are placed around a tungsten converter surrounded by water.

Table 4.2: ^{198}Au activities of gold foils with and without water moderation.

	Activity (μCi)	Activity (water tank) (μCi)	MCNPX Activity (water tank) (μCi)
Top	0.07±0.03	12±3	14
Left	0.08±0.03	15±3	14
Right	0.04±0.02	11±3	14
Back	0.07±0.03	5±2	10

Each foil was counted for one hour after the irradiation. ^{198}Au activities were calculated and are tabulated in Table 4.2 along with the MCNPX predictions. It was found

that the electron beam had shifted to the left. Activities due to photons were similar at all positions in both sets of experiments. However, activities caused by neutrons were higher in the case of the tank full of water, which was expected since neutrons were thermalized. There is a good agreement between the simulation and experimental results.

4.2.3 Neutron Time-of-Flight Measurements

Neutron energies are difficult to measure directly due to the particle's inherent lack of electric charge. A high energy neutron deposits kinetic energy over a large number of collisions. This makes the collection and accurate measurement of its energy a non-trivial exercise. These problems are easily overcome by incorporating a time-of-flight spectroscopy. This method determines neutron energies by measuring the time it takes a neutron to travel a well defined distance. These times are then converted to energy using simple kinematics since the neutron energies in this study are well below relativistic levels.

To benchmark the simulation results and have a better neutron energy spectrum, we tested the IAC's TOF system. The 44 MeV short pulse L-band linac was used for this experiment. Experimental setup and dimensions are shown in Fig. 4.8. The neutron converter and TOF detectors were located in the shielded detection hall. Bremsstrahlung photons were created using a 0.4 cm thick tungsten converter at the 90 degree port of the L-band linac. A magnet was placed right after the converter to divert residue pass-through electrons. The first collimator was placed after that to shape the photon beam prior to entering the experimental cell through a 1.83 m thick shielding wall. The second tungsten target, the neutron converter, was placed at a distance of 1.83 m from the wall. A set of 5 BC-408 detectors were positioned at a height equal to the center of the neutron converter at a distance of 2.6 m from the target. Each detector was isolated using borated polyethylene and the detector set was surrounded by layers of lead to minimize the background noise. The detector set was placed at an angle of $\sim$100 degree with respect to the photon beam vertex to avoid photon flash from the target and collimator.

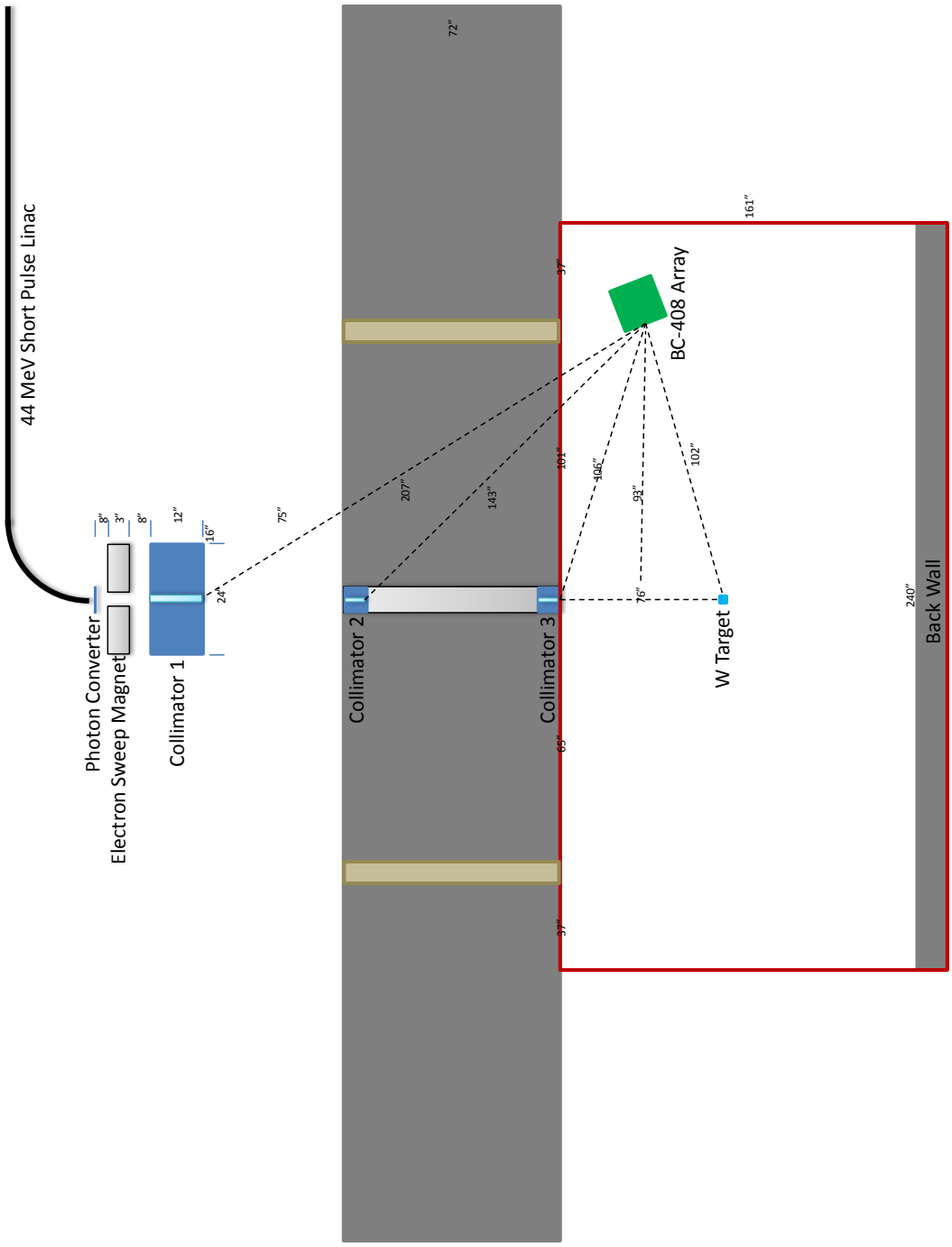

Figure 4.8: Neutron TOF experimental setup and dimensions. [46]

The target was irradiated for one hour using a 30 MeV electron beam (60 Hz, 2 ns pulse-width) to acquire two sets of data with and without the neutron converter. A 6 cm by 6 cm tungsten cylinder was used as a target. Total counts from 5 detectors were summed. The obtained neutron TOF spectrum is shown in Fig. 4.9, where the first three peaks correspond to the photon flashes from collimator 1, the neutron converter, and the back wall, respectively. The last peak corresponds to the neutron flash. The time can be converted to energy using simple kinematics. The neutron energies employed in these experiments are well below relativistic levels, so the energy conversion can therefore be calculated using

$$E_n = \frac{1}{2} M_n \frac{d^2}{(t - t_0)^2}, \tag{4.1}$$

where M_n is the mass of the neutron (939.6 MeV/c^2), d is the flight distance between the points of emission and detection (2.6 m), and t_0 is the time at which the emission occurs.

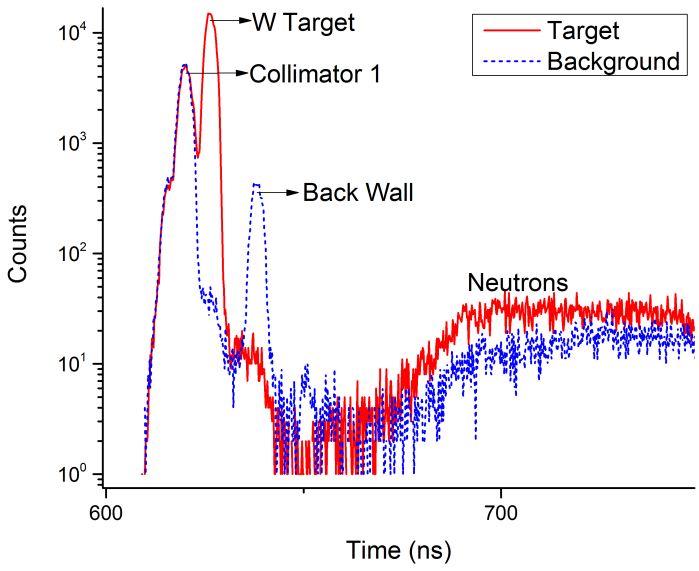

Figure 4.9: Neutron TOF spectrum.

By setting the time of the photon flash peak from the target as the time which the

neutron emission occurs (which found to be t_0=626.2±0.1 ns as shown in Fig. 4.9), we can convert the time spectrum into an energy spectrum.

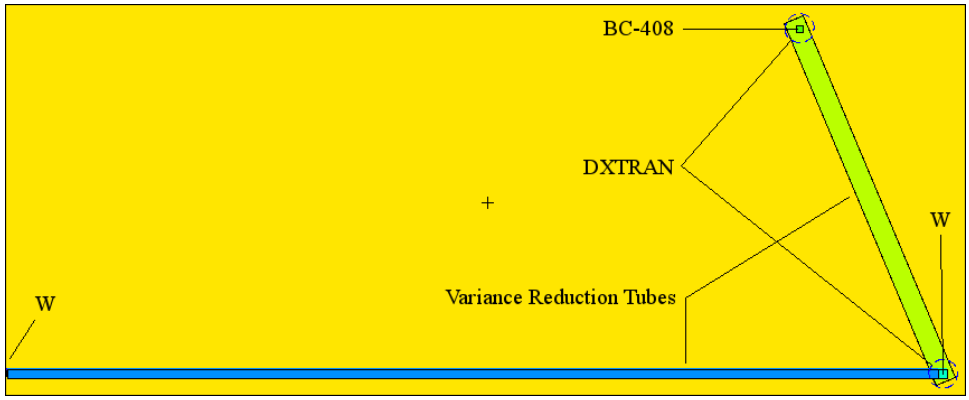

Figure 4.10: MCNPX model of the neutron TOF setup.

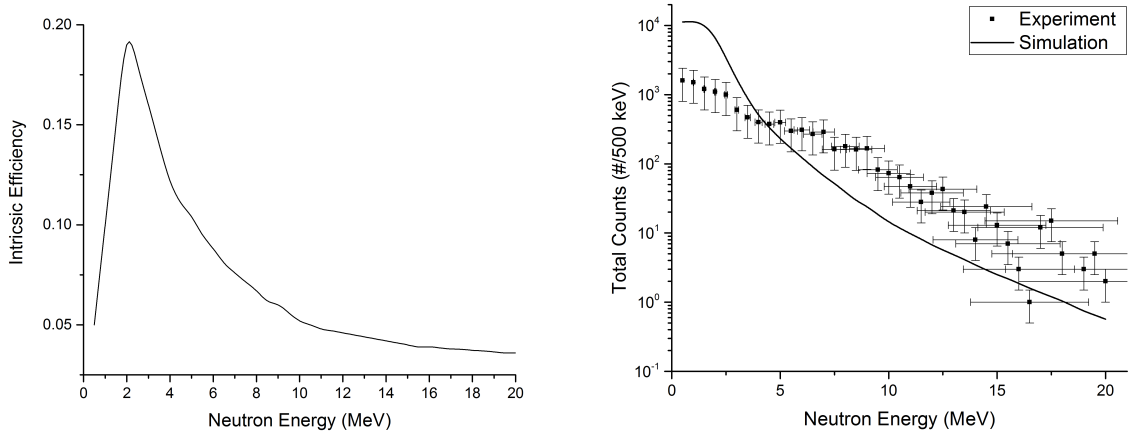

Figure 4.11: BC-408 intrinsic efficiency (left) [49] and neutron TOF energy spectrum from the experiment and simulation (right).

MCNPX simulations were done to benchmark the experimental measurements. Variance reductions techniques were used to minimize uncertainty due to the complexity of the problem and extensive collimation and shielding. The MCNPX simulation setup is

shown in Fig. 4.10. After obtaining the neutron flux spectrum registered in the BC-408 detectors, the results were scaled by the number of detectors and the detector efficiency in Fig. 4.11. The measured and simulated neutron energy spectra are shown in Fig. 4.11. The results show that the two are in good agreement.

4.2.4 Transmutation of LLFP Surrogates

After having radiation fields simulated, we wanted to test out some surrogate materials to address the feasibility of the nuclear waste transmutation technique. RuO_2 powder was used as the surrogate material for ^{99}Tc. An aluminum tank full of water was installed at the end of the beamline. It contained a 1 cm thick Cu-W converter and two sets of samples, Sample 1 and 2. Gold foils were placed right next to each RuO_2 sample for quality assessment (Fig. 4.12).

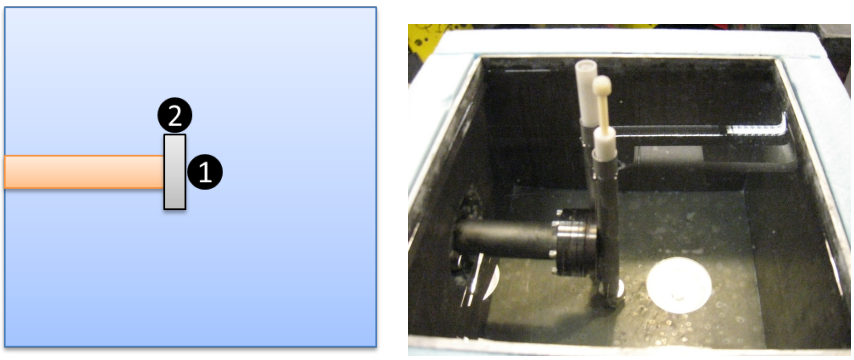

Figure 4.12: RuO_2 and gold foil experimental setup.

The samples in the tank were irradiated for 3 hours using a 330 W, 38 MeV electron beam. The activity of the four isotopes were measured using a HPGe detector. Experimental and simulation results are tabulated in Table 4.3. We can see that the photon induced reactions were greatly suppressed at the sample 2 position. The experimental and simulation results were in good agreement indicating the reliability of MCNPX.

Cesium molybdate (Cs_2MoO_4), which contains ^{133}Cs, was used as a surrogate for ^{129}I.

Table 4.3: Activities of Ru and Au samples.

Isotope	Reaction	Sample 1 Activity (μCi)		Sample 2 Activity (μCi)	
		Experimental	Simulations	Experimental	Simulation
^{103}Ru	^{104}Ru(γ,n)^{103}Ru	1.2±0.4	1.6	0.05±0.02	0.06
^{105}Ru	^{104}Ru(n,γ)^{105}Ru	4.7±0.9	5.4	2.2±0.4	3.1
^{196}Au	^{197}Ru(γ,n)^{196}Au	2.6±0.6	2.8	0.04±0.02	0.5
^{198}Au	^{197}Au(n,γ)^{198}Au	13±2	14	10±2	13

Two sets of experiments were carried out, one using water solution of Cs_2MoO_4, which was kept in sealed plastic bottles surrounded by water, and another experiment was done using polyethylene as the moderator and Cs_2MoO_4 powder. The experimental setup is shown in Fig 4.13. Two tungsten converters were used to make full use of all high energy electrons. One was 1 cm thick and the other one was 6 cm thick. MCNPX simulations were done to visualize neutron and photon fields generated in the tank (Fig. 4.13).

Cesium activities were measured and compared with MCNPX results. A 40 MeV, 10 W electron beam was used for a two hour long irradiation (Table 4.4). The experimental results were verified by the simulation. The results show that the diluted solution based target material reduces the radiation field intensity resulting in a low transmutation rate due to a low concentration of target nuclide.

Table 4.4: Activities of Cs solution samples.

	Experimental (μCi)		MCNPX (μCi)	
	^{132}Cs	^{134}Cs	^{132}Cs	^{134}Cs
1	21±4	0.21±0.05	32	0.4
2	0.02±0.01	0.02±0.01	0.08	0.05
3	0.3±0.1	0.05±0.02	0.4	0.09
4	0.25±0.05	0.04±0.02	0.4	0.09
5	0.015±0.005	0.04±0.02	0.05	0.08
6	0.015±0.005	0.04±0.02	0.05	0.08

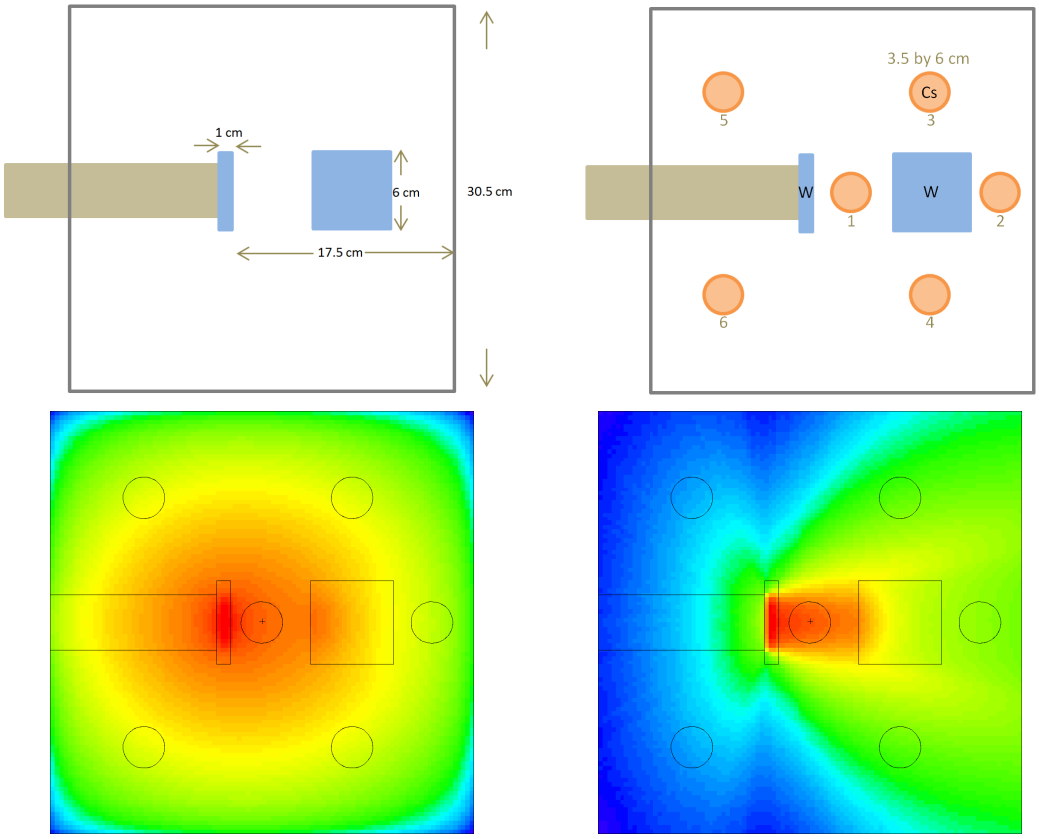

Figure 4.13: Cesium solution experimental setup (top); MCNPX modeled photon and neutron spacial flux distributions (bottom).

4.2.5 ^{47}Sc Production

In Chapter 3, we found that ^{47}Ti(n,p)^{47}Sc reactions do not contribute to the total production yield due to low flux and a moderate neutron absorption cross section. Therefore our final experiment was focused on the photoproduction of ^{47}Sc by (γ,p) reaction. A Ti foil was irradiated to test the production rate. A 22 MeV, 100 W, one hour irradiation was done using a 0.26 cm thick tungsten converter.

A 22 MeV electron beam energy was chosen such that ^{44}Sc production can be suppressed. Simulation and experimental measurements were tabulated in Table 4.5. The production rates align with the simulation results discussed in Chapter 3. The total ac-

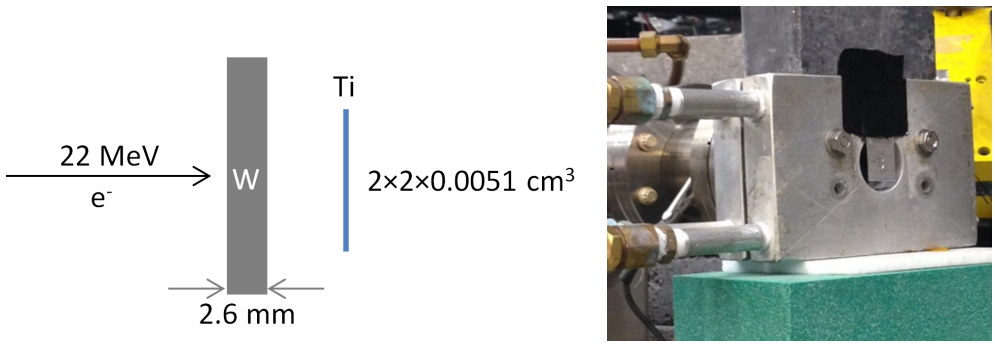

Figure 4.14: ^{47}Sc irradiation setup.

tivity of ^{47}Sc is about 0.6 μCi/g after a one hour irradiation using a 22 MeV electron beam with 100 W of beam power. These results also agree with other ^{47}Sc production studies [50].

Table 4.5: Experimental results of ^{47}Sc production.

Reaction Type	^{47}Ti(γ,p)^{46}Sc	^{48}Ti(γ,p)^{47}Sc	^{49}Ti(γ,p)^{48}Sc
Experimental foil (μCi/g)	0.02±0.01	**0.5**±0.2	0.09±0.04
MCNPX foil (μCi/g)	0.035	**0.61**	0.16
MCNPX Cylinder (μCi/g)	0.032	**0.51**	0.11

Chapter 5

Conclusion and Projections

The goal of this work was to investigate the feasibility of using single and mixed (photon and neutron) fields generated by electron linacs for nuclear transmutation. In particular, we wanted to verify whether either of the above fields can be used for LLFP burnup and radioisotope production, and if so, which one results in the highest reaction rates.

After careful consideration and investigation of field production conditions using Monte-Carlo simulation tools, an optimum bremsstrahlung converter was designed, built, and tested. Copper foils were activated to benchmark photon field generated by the optimized converter and their activity was found to be in good agreement with the simulation results.

Optimization of the photon converter was followed by neutron production studies, both fast and thermal. Again, Monte-Carlo methods were used to find an optimum neutron-production setup. Resulting neutron fields were experimentally verified with aluminum, manganese, gold, and ruthenium samples.

Finally, based on the result of pure gamma and pure neutron converters' optimization, a mixed field converter was designed to provide significant neutron flux in addition to photon flux. It was shown that for certain reactions, mixed field converter was beneficial. Monte-Carlo simulation results were benchmarked using cesium samples.

Two practical examples were investigated: LLFP burnup and radioisotope production. It was shown that significant burnup rates can be achieved using mixed field irradiation of ^{129}I, one of the most radiotoxic components of LLFP. As far as the isotope production is concerned, two cases were investigated. ^{47}Sc production from Ti was shown to have the

highest yield using pure gamma irradiation. On the other hand, ^{64}Cu production yield improved significantly by using mixed field irradiation in comparison to the single gamma field.

5.1 Radiation Field Production

Numerous experiments and computer simulations have been conducted to assess the spacial distribution and field intensity of photon and neutrons. Effects of the electron beam parameters, target and converter setup, and irradiation conditions have been addressed to find optimum field production. Fig. 5.1 summarizes field production capabilities using electron accelerators with different beam energies. Both photon and neutrons fields were optimized for each beam energy. Overall, regardless of beam energy, photon fluxes significantly exceed neutron fluxes. While neutron fluxes generated by linacs cannot compete with photon fluxes (without using fissionable materials), for many reactions, neutron contribution to reaction rate can be significant and reach tens of percent.

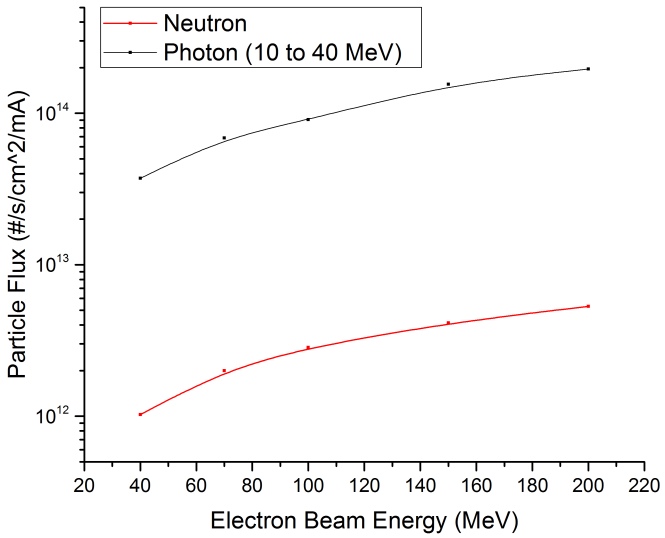

Figure 5.1: Average photon and neutron flux over a volume of 10×10×10 cm^3.

Although Fig. 5.1 represents results Monte Carlo simulations, 40 MeV data points were experimentally verified at the Idaho Accelerator Center (IAC).

5.2 Fission Product Transmutation

In order to investigate the feasibility of a realistic nuclear waste transmutation method, activity measurement routines and various operating schemes have been investigated. With the aid of simulation codes and experiments, an optimum transmutation experimental design, along with particle flux distributions, were outlined and summarized in Chapter 3. Two converters were used for photon and neutron production with target material circulating through the channel surrounded by water moderator. This setup is optimum such that both photon and neutron fields are utilized effectively.

As was pointed out in Chapter 1, ^{99}Tc and ^{129}I contribute the most to the radiotoxicity of LLFP. Tc and I are amenable to photon, neutron, and mixed field transmutation. Part of the motivation for this work was to examine, in principle, the possibility of using photon induced reactions to transmute these nuclides. It has been shown that, indeed, these processes can provide transmutation at some level for iodine. One way to assess the practicality of such a method is to look at the transmutation rate addressing the cost in electric power. ^{129}I(γ,n)^{128}I and ^{129}I(n,γ)^{130}I reaction rates have been calculated using photon only, neutron only, or mixed-field of both. Single converters were used for a single radiation field optimization (as mentioned in the Section 3.2 and 3.3). Two converters were used for the mixed-field optimization (Section 3.5.2).

With the optimum design conditions for each scenario, burn-up rate of ^{129}I has been calculated for different electron beam energies and powers (Fig.5.2). We can see that the most cost effective transmutation of ^{129}I is achieved with a 70 MeV electron accelerator when using photon-only field. This is to say that excessive photons are wasted when using a higher energy electron beam since only about 10 to 30 MeV photons are useful. The most cost effective transmutation by neutron-only field is achieved by using around

100 MeV electron beam linac. A higher energy electron beam is also needed to reach a better transmutation rate by mixed radiation field (around 100 MeV). Note that the sum of neutron and photon single field induced transmutation rates is greater than that of the mixed-field transmutation rate because optimization of both neutron and photon fields comes at a cost of sacrificing the maximum production of single fields.

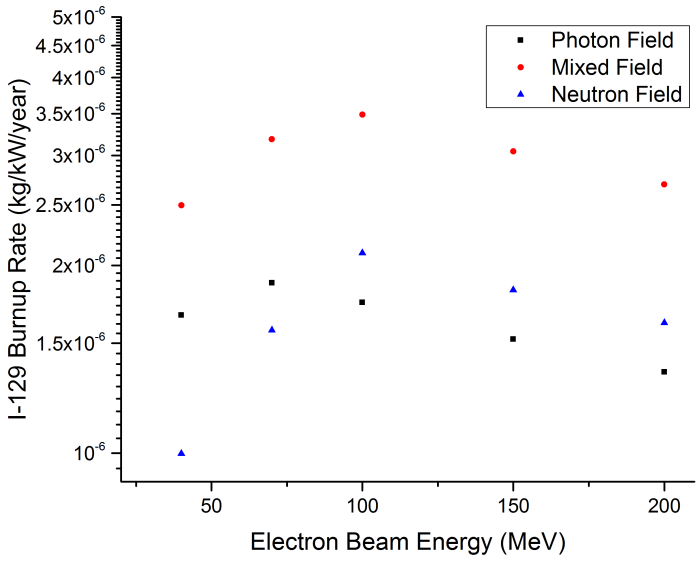

Figure 5.2: ^{129}I burnup rate.

Assuming the annual generation of ^{129}I by, say, a 1 GWt (Giga Watt thermal) LWR (Light Water Reactor)(300 MWe (Mega Watt electric)) in one year to be about 2 kg, we can calculate, based on our results in Fig. 5.2, the transmutation rates. They were found to be 0.0034, 0.0041, and 0.007 kg for a 1 MW electron accelerator in a year for photon, neutron, and mixed field irradiation schemes, respectively.

The simulation and experimental data were obtained for a very simple converter/target designs. A more complex system could potentially increase the total amount of material to the transmuting field. An example of such improved scheme is shown in Fig. 5.3. This scheme can improve the dual field method by a factor of 5 comparing to the mixed-field

burn-up rate showed in Fig. 5.2. Further exploration of these possibilities is beyond the scope of this dissertation but will be the subject of future work. Electron accelerator based burn-up of ^{99}Tc can possibly lead to photoproduction of ^{98}Tc, so it needs to be carefully designed.

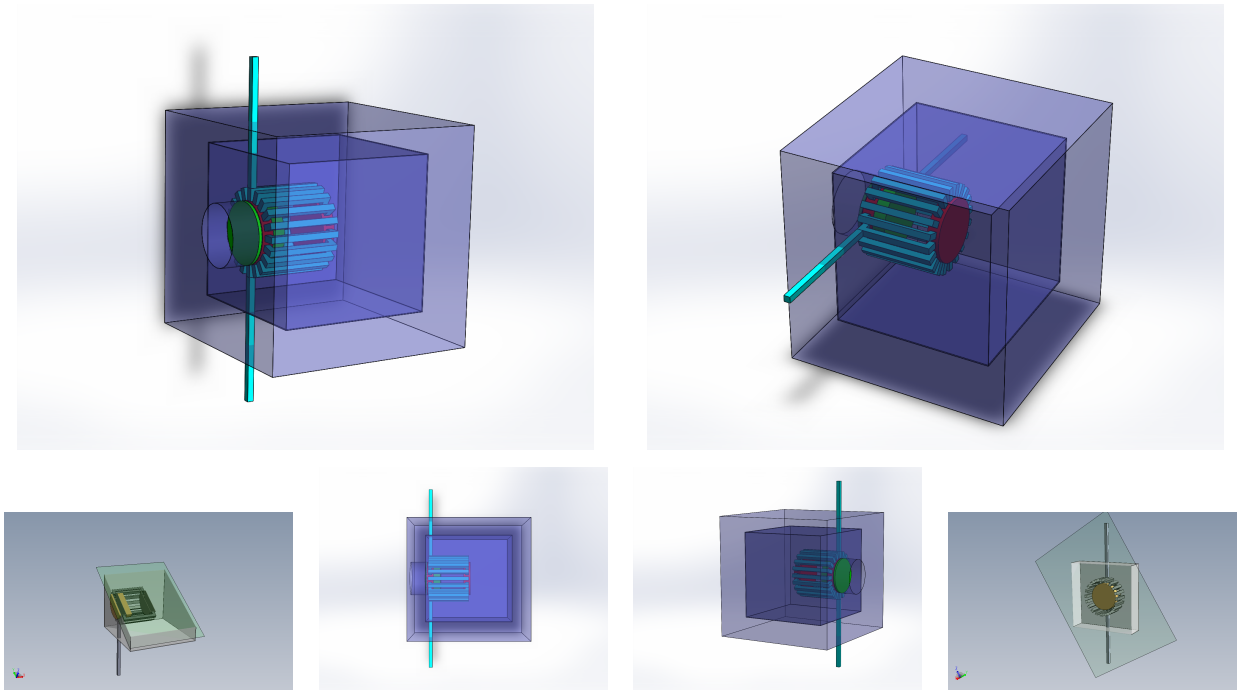

Figure 5.3: An example of a more complex design cell for the electron accelerator based nuclear waste transmutation technique. In this design, two tungsten converters were used. Aqueous solution or molten salt containing target nuclides can be pumped in and can be circulated through the tubes in a box filled with water. Beryllium reflector surrounds the water tank.

5.3 Radioisotope Production

While the results of the work with Sc showed that no increase in yield could be obtained by using the mixed-field radiation scheme, photoproduction of ^{47}Sc was proven

to be quite effective. Like most other medical radioisotopes, ^{47}Sc samples require high purity and high specific activity. To achieve it, the target material needs to be enriched (^{48}Ti) and an efficient separation scheme of Sc from Ti needs to be developed. Using the optimization methods discussed in Chapter 3, maximum ^{47}Sc production yields for different electron beam energies are shown in Fig. 5.4 (left). Byproduct (^{46}Sc) yields are also shown as major impurity.

^{64}Cu production can significantly benefit from the mixed-field irradiation due to its nuclear properties. It was shown in Chapter 3 that mixed-field irradiation increases ^{64}Cu yield by about 30%. Note that a considerable amount of ^{62}Cu and ^{66}Cu will be produced by (γ,n) and (n,γ) reactions from ^{63}Cu and ^{65}Cu, respectively. However, due to their extremely short half-lives (9.74 m and 5.1 m correspondingly), ^{62}Cu and ^{66}Cu production can be ignored. Waiting for 30 minutes to an hour after irradiation will eliminate this problem. Maximum production yields of ^{64}Cu using linacs of different energies are shown in Fig. 5.4.

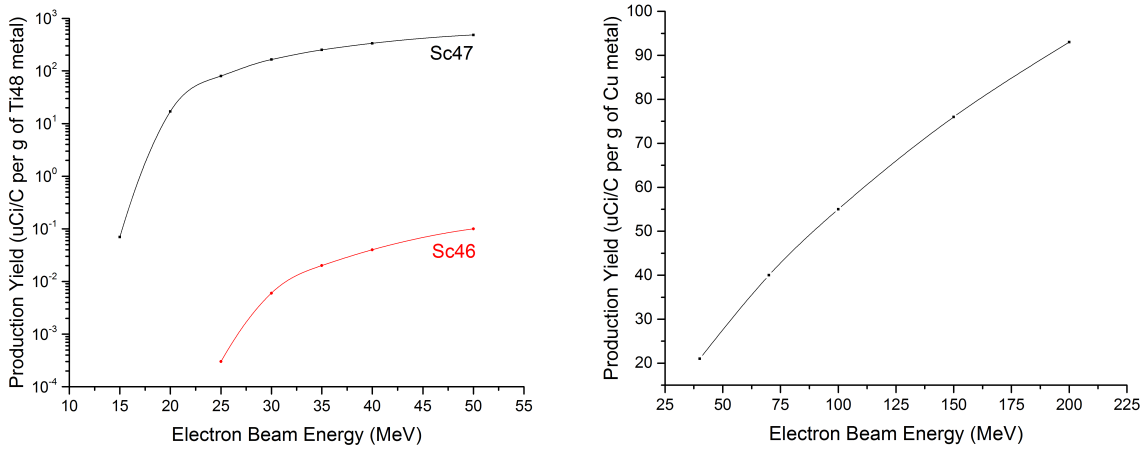

Figure 5.4: Isotope production rates.

For both scandium and copper, much more work is necessary to address the issues of increasing the purity and specific activity of the isotope, as well as scaling up the

production setup which is far beyond the scope of this thesis. Our goal was to just show that the mixed field concept can be applicable not only for nuclear waste transmutation, but for isotope production as well. We have demonstrated that, in some cases, using mixed field might result in higher yields in comparison with the single field irradiation

References

[1] E. Haug, W. Nakel, "The Elementary Process of Bremsstrahlung," *World Science,* Vol. 73, 2004.

[2] C.R. Segebade, H.P. Weise, and G.J. Lutz, *Photon Activation Analysis,* Walter de Gruyter, Berlin, New York, 1988. ISBN: 3-11-007250-5

[3] Mayir Mamtimin, "Feasibility Study of Photon Activation Analysis on Airborne Particulates , Volcanic Ash, and Moon Dust Simulants," Master Thesis, Idaho State University, 2011.

[4] Z.J. Sun, "Photon activation analysis and the provenance study of coffee," PhD Dissertation, Idaho State University, 2011.

[5] R.J.M. Konings, J.L. Kloosterman, J.A. Hendricks, and H. Gruppelaar, "Transmutation of Technetium in the Petten High Flux Reactor: A Comparison of Measurements and Calculations," *Nuclear Science and Engineering,* 128, 70-75, 1998.

[6] C. Ingelbrecht, J. Lupo, K. Raptis, T. Altzitzoglou, and G. Noguere, "^{129}I targets for studies of nuclear waste transmutation," *Nuclear Instruments and Methods in Physics Research A,* 480, 204-208, 2003.

[7] Yaxi Liu, Man-Sung Yim, David McNelis, "Comparison of Neutron Yield Characteristics between Proton Accelerator and Electron Accelerator for Waste Transmutation," *Advanced Nuclear Energy Systems Research and Development.*

[8] Yaxi Liu, "A study on the feasibility of electron-based accelerator driven systems for nuclear waste transmutation," PhD dissertation. North Carolina State University, 2006.

[9] CERN-SL-99-036- EET, "Neutron-Driven Nuclear Transmutation by Adiabatic Resonance Crossing," *European Organization for Nuclear Research,* The TARC Collaboration. Geneva, July, 1999.

[10] J.G. Chen, W. Xu, H.W. Wang, W. Guo, Y.G. Ma, X.Z. Cai, and G.C. Lu, "A potential photo-transmutation of fission products triggered by Compton backscattering photons," *Nuclear Instruments and Methods in Physics Research A,* pp. 118-123. 2009.

[11] H. Nifenecker, O. Meplan and S. David *Accelerator Driven Subcritical Reactors*, IOP Publishing Ltd 2003.

[12] A.S. Gerasimov, T.S. Zaritskaya, G.V. Kiselev, and L.A. Myrtsymova, "The Cost of Transmutation of Fission Products in Nuclear Reactors," *Atomic Energy,* Vol. 94, No. 3, 2003.

[13] S. M. Seltzer and M. J. Berger, "Photoneutron Production in Thick Targets," Physical Review C, Vol. 7, Num. 2, 1973

[14] M. Salvatores and G. Palmiotti, "Radioactive waste partitioning and transmutation within advanced fuel cycles," *Progress in Particle and Nuclear Physics,* 2010.

[15] V. Makarashvili, S. Chemerisov, and B. Micklich, "Simulations of a LINAC-based photoneutron source," *Nuclear Instruments and Methods,* 2012.

[16] W.S. Yang, Y. Kim, R.N. Hill, T.A. Taiwo, and H.S.Khalil, "Long-Lived Fission Product Transmutation Studies," *Argonne National Laboratory, Nuclear Engineering Division,* June 2003.

[17] Waclaw Gudowski, "Transmutation of Nuclear Waste," *Royal Institute of Technology,* Stockholm, Sweden.

[18] Kenji Nishihara and Hideki Takano, "Transmutation of ^{129}I using an Accelerator-driven System," *Radioactive Management and Disposal,* July, 2001.

[19] Valeriia Starovoitova, Douglas P. Wells, "Cu-67 photonuclear production," *AIP Conference proceedings,* vol. 1336, pp. 502-504 (2011)

[20] Y. Danon, R. Block, and J. Harvey, "Production of Mo-99 Using 30 MeV Electron and a Mo-100 Target," *Reactor- and Accelerator-Based Production of Mo-99.*

[21] S. James and Frederick J. Manning, "Isotopes for Medicine and the Life Science," *National Academy Press,* 1995

[22] V. B. Berestetskii, E. M. Lifshitz, and L. P. Pitaevskii, "Quantum Electrodynamics," *B. H.,* 1971

[23] R. P. Feynman, "Quantum Electrodynamics," *W. A. Benjamin, INC.,* 1961

[24] Bruno Rossi and Kenneth Greisen, "Cosmic-Ray Theory," *Reviews of Modern Physics,* Volume 13, Oct, 1941.

[25] Walter Heitler, "The Quantum Theory of Radiation," *Courier Dover Publications,* 1954

[26] J.D. Jackson, *Classical Electrodynamics,* John Wiley & Sons, New York, 3rd Edition, 1999

[27] H. Bethe and W. Heitler, "On the Stopping of Fast Particles and on the Creation of Positive Electrons," *Proc. R. Soc. Lond. A,* 146, 1934

[28] J. F. Carlson and J. R. Oppenheimer, "On Multiplicative Showers," Physical Review, vol. 51, p 220-231, 1937

[29] Douglas P. Wells, "Elastic Photon Scattering from He-4 between 23 and 73 MeV," PhD Thesis, University of Illinois, 1990.

[30] B.L. Berman and S. Fultz, "Measurements of The Giant Dipole Resonance with Monoenergetic Photons," *Reviews of Modern Physics*, 47, pp, 713–761, 1975.

[31] B. Rossi, "High Energy Particles," (Prentice-Hall, New York, 1952), p. 244.

[32] John Hendricks, Randy A. Schwarz, *MCNP/MCNPX Intermediate Workshop.* Las Vegas, Nevada, 2013

[33] P. Rinard, "Neutron Interactions with Matter."

[34] Monte Carlo N-Particle eXtended. Los Alamos National Laboratory. (mcnp.lanl.gov)

[35] M.C. White, R.C. Little, and M.B. Chadwick. "Photonuclear Physics in MCNP(X)," *Proceedings of the ANS on Nuclear Applications of Accelerator Technology,* Long Beach, California, Nov. 14-18, 1999.

[36] Kevin Folkman, Chad O'Neill, Brian Berls. The courtesy of IAC engineers.

[37] P. V. Mikhailovich, E. A. Dmitrievich, K. F. Alekseevich, O. Y. Ivanovich, and S. A. Pavlovich, "Liquid Metal Coolants Technology for Fast Reactors," Journal of Materials Science and Engineering B 1 913-928, 2011

[38] J. J. Park, D. P. Butt, and C. A. Beard, "Potential Containment Materials for Liquid-Lead and Lead-Bismuth Eutectic Spallation Neutron Source," LALN, 1997

[39] V.C. Petwal, V.K. Senecha, K.V. Subbaiah, H.C. Soni and S. Kotaiah, "Optimization studies of photo-neutron production in high-Z metallic targets using high energy electron beam for ADS and transmutation," *Indian Academy of Science,* Vol. 68, No. 2, Feb 2007, PP. 235-241.

[40] K.G. Dedrick and H.H. Clark, "Photoneutron Yields from Excitation of the Giant Resonance," Sep, 1960.

[41] Xiaotian Mao, Kenneth R. Kase, and Walter R. Nelson, "Giant Dipole Resonance Neutron Yields Produced by Electron as a Function of Target Material and Thickness," SLAC-PUB-6628, 1996

[42] Gleen A. Price, "Energy Spectra and Angular Distribution of Photoneutrons from Heavy Nuclei," Physical Review, Volume 93, Number 6, 1954.

[43] Tabbakh Farshid and Khalafi Hossein, "Target Optimization for a 10-MeV E-beam Neutron Converter," Nuclear Science and Techniques 21 (2010) 69-71

[44] Idaho Accelerator Center. (iac.isu.edu)

[45] Mark Bulzer, The courtesy of IAC radiation engineer.

[46] Heather Seipel and Edward Reedy. The courtesy of IAC research assistants.

[47] S.C. Fultz, "Handbook on photonuclear data for applications cross-sections and spectra," IAEA, 2000.

[48] A.J. Koning and D. Rochman, "TALYS-based Evaluated Nuclear Data Library," *Nuclear Research and Consultancy Group.* Nov, 2009, 2011.

[49] S. J. Thompson, "A High-Energy Prompt Neutron Signature for the Detection of Fissionable Materials," PhD Dissertation, Idaho State University, 2010.

[50] Masuo Yagi and Kenjiro Kondo, "Preparation of Carrier-free ^{47}Sc by the ^{48}Ti (γ,p) Reaction," Lab. of Nuc. Sci., 982, Japan, 1976

Appendix A

Error Analysis

A.1 Computer Simulation

MCNPX has built in statistical check cards to ensure the reliability of the results. By using different variance reduction methods, each set of simulations were performed until the statistical errors were less than 5%. For the reaction yield or activity calculations by FM cards, MCNPX does not include the uncertainty in the cross section data. In general, cross section contributes an average of 5% for a well-known reaction type (Fig. B.5). Therefore, all the particle flux simulations results were subject to a maximum of 5% and all the reaction yield calculations were subject to a maximum of 7% uncertainty.

A.2 Experimentation

Yield measurements were performed by measuring net peak counts by the gamma-spectrometer. Reciting Eqn. 2.29 from Chapter 2:

$$P(T_i, T_d, T_c) = \frac{M\mathcal{A}\mathcal{N}_A\varepsilon\mathcal{P}_\gamma}{A_r\lambda}(1 - e^{-\lambda T_i})e^{-\lambda T_d}(1 - e^{-\lambda T_c}) \int_{E_{th}}^{E_{\max}} \Phi(E)\,\sigma(E)\,dE. \qquad \text{(A.1)}$$

This quantity is effected by the uncertainties of the sample mass (1%), detector efficiency (10%), irradiation, decay, and counting time duration (1%), electron beam energy (10%), and beam current (5%). Uncertainty in quantities such as natural abundance, Avogadro's constant, gamma emission probability, relative atomic mass, and decay half-life can be

neglected. Therefore the propagated uncertainty can be calculated as

$$\frac{\sigma_P}{P} = \sqrt{\left(\frac{\sigma_M}{M}\right)^2 + \left(\frac{\sigma_\varepsilon}{\varepsilon}\right)^2 + 3 \cdot \left(\frac{\sigma_T}{T}\right)^2 + \left(\frac{\sigma_E}{E}\right)^2 + \left(\frac{\sigma_I}{I}\right)^2} = 0.15. \tag{A.2}$$

Gamma spectroscopy has statistical uncertainty of 5%. So all the experimental results of activity calculations were subject to a uncertainty of 20%.

For neutron TOF energy measurements, the main sources of uncertainty are in the time of flight and number of registered counts. Time resolution is the direct determining factor in the timing uncertainty. There are several components effecting the time resolution of a scintillator crystal, the photomultiplier tube, and the electronics. Timing resolution of BC-408 is about 0.2 ns which contributes about 0.1 to 1% in the energy resolution from low keV to MeV. However, uncertainty introduced by the electronics range from 5 to 10 % depending on the neutron energy. Therefore, uncertainty in the neutron energy measurement is

$$\frac{\sigma_t}{t} = \sqrt{2 \cdot \left(\frac{\sigma_R}{R}\right)^2 + \left(\frac{\sigma_J}{J}\right)^2} = 0.16. \tag{A.3}$$

Uncertainty in the detector counts is

$$\frac{\sigma_P}{P} = \sqrt{\left(\frac{\sigma_\varepsilon}{\varepsilon}\right)^2 + \left(\frac{\sigma_E}{E}\right)^2 + \left(\frac{\sigma_I}{I}\right)^2} = 0.15. \tag{A.4}$$

Adding a statistical error of 5%, the overall counting uncertainty is about 20%.

Appendix B

Additional Plots

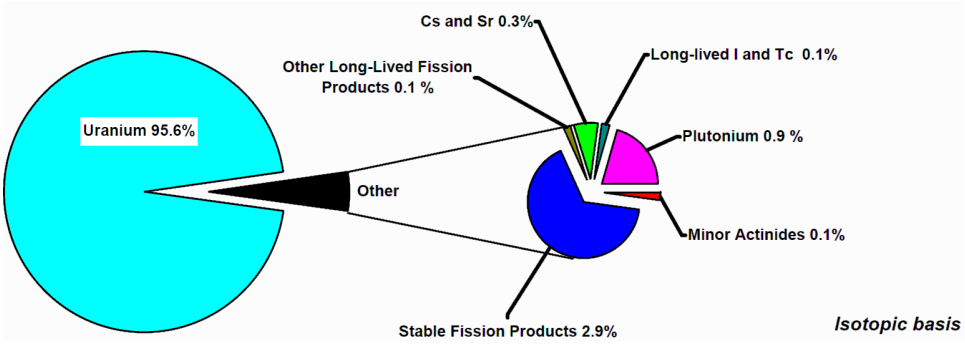

Figure B.1: Constituents of spent fuel. [14]

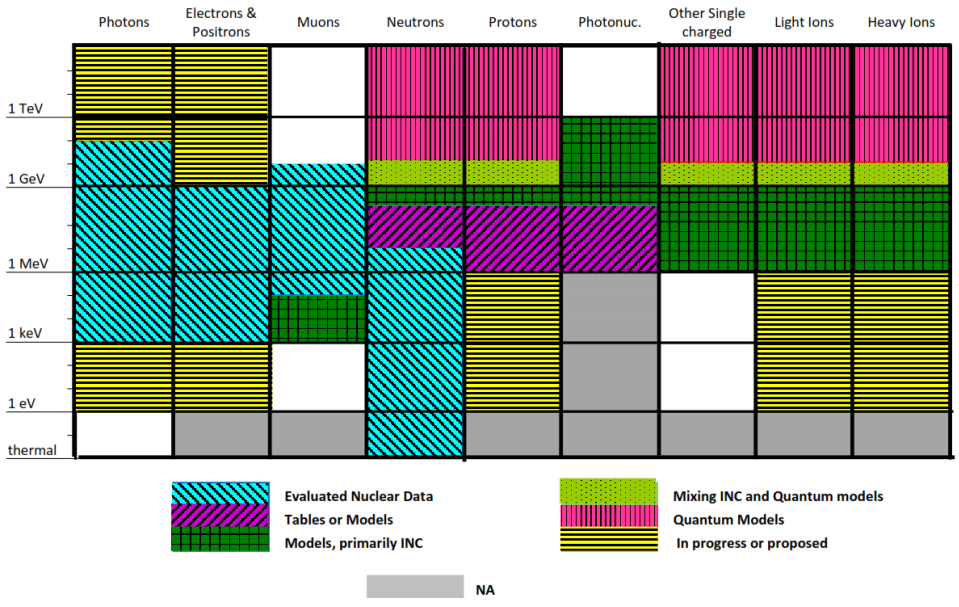

Figure B.2: Physics coverage of MCNPX. [32]

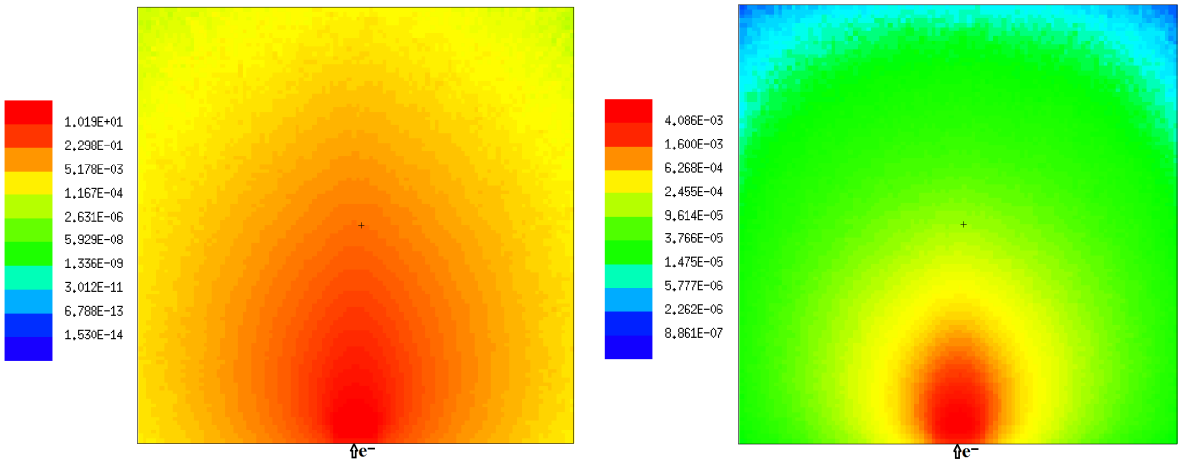

Figure B.3: Spacial distribution of photon and neutron field in a 10 cm by 10 cm W block.

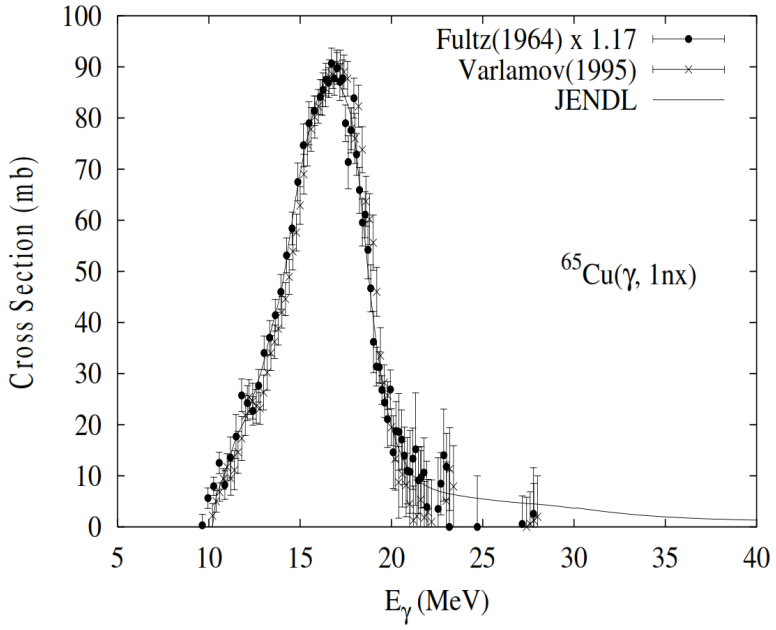

Figure B.4: ^{65}Cu(γ,n)^{64}Cu reaction cross section. [48]

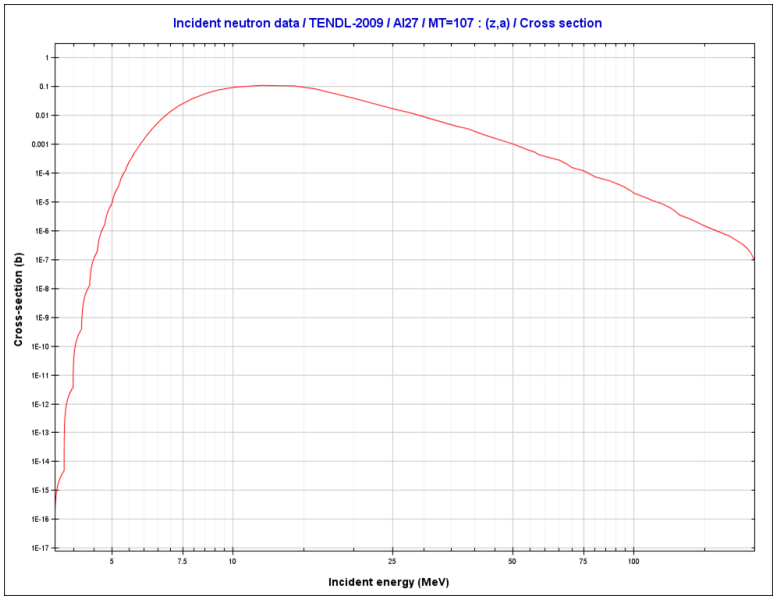

Figure B.5: Model cross section of ^{27}Al(n,α)^{24}Na. [48]

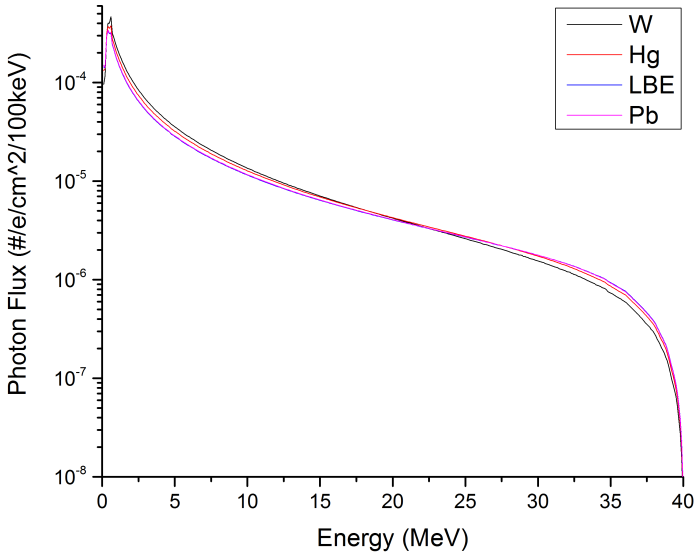

Figure B.6: Photon flux density produced by different material.

Appendix C

A Sample MCNPX Input File

```
Converter type vs neutron yield
$Cell Cards
1 4 -19.25 -1
2 4 -19.25 -2
3 0 -3 2 1
4 0 3

$Surface Cards
1 rcc 0 0 0 0.35 0 0 5
2 rcc 0.35 0 0 1 0 0 10
3 rcc -5 0 0 30 0 0 11

$Data Cards
mode p e n
m4 74000.70c -1  $19.25
imp:p,e,n 1 2r 0
phys:e 5j 20 j 0
phys:p 3j 1
sdef pos -4.5 0 0 rad d1 ext d2 axs 1 0 0 dir 1.0 vec 1 0 0 par e erg=40
si1 0 0.1
sp1 -21 1
si2 0 4
sp2 -21 0
cut:p j 1.6
cut:e j 1.6
print
c prdmp j 1e8 1 3 1e8
nps 1e9
f14:n 2
e0 0.001 999ilog 40
```